Synergising Local Geo-Environmental Characteristics with Spatial Context for Enhancing Landslide Susceptibility Mapping

Yusen Cheng[1, 2], Lei Fan[1, *], Qinfeng Zhu[1, 3], Cheng Zhang[1], Yangyang Li[4, 5], Ron Mahabir[2]

[*] *Correspondence: Lei Fan (Lei.Fan@xjtlu.edu.cn)

[1] Department of Civil Engineering, Xi'an Jiaotong-Liverpool University, Suzhou, 215123, China

[2] Department of Geography and Planning, University of Liverpool, Liverpool, L69 3BX, UK

[3] Department of Computer Science, University of Liverpool, Liverpool, L69 3BX, UK

[4] Suzhou Industrial Park Monash Research Institute of Science and Technology, Monash University, No. 1 Huayun Road, SIP Suzhou, 215000, PR China

[5] Department of Civil Engineering, Monash University, 23 College Walk, Clayton, Victoria 3800, Australia

Abstract

Data-driven methods are widely used in landslide susceptibility mapping (LSM) because they can effectively model the complex relationships between landslides and geo-environmental conditions. Existing data-driven approaches generally follow two types of data representations. Pixel-based models focus solely on the geo-environmental characteristics of a specific landslide but neglect the influence of its surrounding environment. Patch-based models incorporate surrounding spatial context but may include pixels with weak or no spatial relevance to the target landslide location. To address this limitation, this study proposes a Local-Geo and Spatial Context Fusion (LGSCF) strategy, which synergises the geo-environmental characteristics of landslide points with their corresponding spatial context through a feature-wise modulation mechanism. We tested the LGSCF strategy by integrating it into several representative convolutional neural network (CNN) architectures, creating nine different LGSCF-based models. The primary study area covers approximately 2644 km² across Jenai and Sinyi Townships in Nantou County, Taiwan, and the dataset comprises 5332 landslide samples and an equal number of non-landslide samples. The results show that LGSCF-based models consistently outperform their corresponding baselines, achieving F1-scores up to 87.09% and AUC values up to 0.9472. Furthermore, the susceptibility maps produced by LGSCF-based models show that known landslides are more accurately concentrated in "very high" susceptibility zones with fewer misclassifications. These findings demonstrate that our fusion strategy can significantly improve the accuracy of landslide susceptibility mapping.

Keywords: Landslide; Prediction; Landslide susceptibility; Feature fusion; Deep learning; Convolutional neural network

1 Introduction

Landslides are downslope movements of rock, soil, or debris driven by gravity, commonly triggered by intense rainfall, earthquakes, volcanic activity, or human interventions [1], posing severe threats to both mountainous and densely populated urban regions [2,3]. In recent decades, the frequency of landslide disasters has shown a clear increase [4], closely associated with the combined effects of climate change and intensified human activities such as deforestation, slope modification, and unplanned urban expansion. These events often result in severe consequences, including loss of life, damage to infrastructure, and widespread socio-economic disruption [5,6]. Hence, accurate prediction of landslide-prone areas has become a crucial element of disaster prevention and mitigation, providing critical spatial insights for land-use planning and timely risk reduction.

In response to this need, landslide susceptibility mapping (LSM) has become one of the primary approaches. LSM refers to the delineation of spatial zones with different levels of susceptibility to landslides by analysing the relationship between historical landslide occurrences and landslide geo-environmental conditioning factors (LCFs) such as topography, geology, vegetation, and rainfall. The underlying assumption is that future landslides are more likely to occur under environmental conditions similar to those of past events. Over the years, LSM has transitioned from qualitative assessments based on expert knowledge and heuristic evaluations [7,8] to semi-quantitative approaches using statistical indices and weighted overlays [9,10]. More recently, with the advancement of data availability and computational techniques, quantitative methods have represented the prevailing practice [11ï 13]. Quantitative methods can be broadly divided into physically based and data-driven approaches. Physical models typically rely on geomechanical and hydrological principles of slope stability and are capable of providing detailed process-level insights, making them valuable in site-specific engineering practice. However, their application in regional-scale LSM is constrained by several factors, such as the difficulty of acquiring accurately measured soil and hydrological parameters [14,15], a focus on a single failure mechanism rather than diverse landslide types [16], and the high computational demand [17].

Given the ability and flexibility in handling diverse LCFs and in operating on landslide inventories from multiple sources, machine learning methods constitute the most widely applied category of data-driven approaches in LSM. Commonly used algorithms include logistic regression (LR) [18,19], support vector machines (SVM) [20,21], naµve Bayes [22,23], random forests (RF) [24,25], and k-nearest neighbours (KNN) [26,27]. In recent years, the application of machine learning in LSM has not only achieved consistently high prediction accuracy [28,29], but also provided insights into the relative importance of LCFs and the underlying mechanisms of slope failure through

interpretability techniques [30,31]. Despite these strengths, machine learning models typically use raw or discretised LCFs as input features without extracting hierarchical representations to capture complex patterns. Moreover, when pixel units are adopted, classification is generally based only on the attributes of the landslide or non-landslide pixel itself, neglecting the spatial context of surrounding areas. These may lead to unstable predictions along slope boundaries and reduce the modelôs ability to capture terrain continuity and hydrological connectivity, thereby limiting the potential for further performance gains.

To address these limitations, Wang et al. [32] were the first to introduce deep learning into LSM, testing four different convolutional neural network (CNN) architectures (CNN1D, CNN2D, CNN3D, and LeNet-5) and reporting promising performance. Since then, CNN-based methods have been increasingly adopted in landslide studies and have frequently outperformed conventional machine learning approaches in terms of predictive accuracy [33ï 35]. From the perspective of input data representation, these methods can be broadly grouped into the following two categories.

The first category directly encodes the LCFs of landslide or non-landslide points without explicitly incorporating neighbourhood context. In this case, the LCFs of a sample are arranged as a one-dimensional array, with each feature placed sequentially along the same axis, or transformed into two-dimensional tensors after discretisation and reorganisation of categorical and continuous factors [36ï 38]. Although such CNN designs allow models to extract hierarchical representations and capture complex nonlinear relationships, they still rely solely on pixel-level attributes and therefore overlook the spatial context of surrounding conditions.

The second category expands around each landslide or non-landslide point to construct patch-based samples with dimensions $n \times n \times c$, where n denotes the patch size, and c is the number of LCFs. This approach incorporates spatial context by including both the central pixel and its neighbouring environment [39ï 41]. Nevertheless, it inevitably introduces redundant information, as not all surrounding pixels are equally relevant to slope failure. Due to the nature of CNN operations, successive convolution and pooling layers can progressively aggregate neighbourhood signals and downsample the feature maps, so the contribution of the central pixel, which directly corresponds to the class label, may become blurred or diluted. Furthermore, although the final fully connected (FC) layers can learn nonlinear combinations and implicitly weight features, they lack an explicit mechanism to prioritise critical information or to condition the spatial representation accordingly. As a result, the model may be overly influenced by irrelevant background features while underutilising the most informative cues. These limitations have motivated two related directions in recent LSM research: applying architectures that can model broader spatial dependencies and

designing fusion mechanisms that can integrate complementary representations more effectively.

Recent transformer and graph-based approaches primarily reflect the first direction. Vision Transformers (ViTs) treat image patches as tokens and use self-attention to capture long-range interactions, although their performance may be constrained by the limited training samples typical of LSM [42]. Hybrid CNNï Transformer models combine the extraction of terrain patterns by CNNs with transformer-based global-context modelling [43,44]. Graph neural networks (GNNs), by contrast, represent slope units or environmentally related locations as nodes and encode their spatial or environmental relationships as edges, allowing information to propagate between adjacent or similar terrain units [45ï 47]. These approaches extend the spatial modelling capability of conventional CNNs, but they mainly focus on feature extraction and dependency modelling rather than explicitly coordinating the roles of local environmental attributes and surrounding geospatial context.

The second direction concerns how complementary representations are fused. In remote sensing, heterogeneous information can be combined at the input, intermediate-feature, or decision level [48]. At the feature level, fusion strategies range from direct concatenation or summation to learned feature recalibration. Squeeze-and-excitation (SE) and convolutional attention modules learn channel-wise and/or spatial weights to emphasise informative responses [49,48], whereas transformer-based approaches use self-attention or cross-attention to model long-range and cross-source dependencies [50]. However, these methods are not specifically designed to address a particular challenge in point-centred, patch-based LSM: the central pixel represents the location to be classified, whereas the surrounding patch provides contextual information whose relevance may vary according to the local geo-environmental conditions. Thus, the two inputs are not interchangeable modalities, but two representations of the same LCF data at different spatial scopes.

To address the issues, this study proposes a Local-Geo and Spatial Context Fusion (LGSCF) framework that synergises pixel-level geo-environmental characteristics with their surrounding spatial context. Specifically, the local-geo branch encodes the geo-environmental characteristics of the central pixel, corresponding to the location of a landslide or non-landslide point, while the spatial-context branch captures spatial patterns from the entire image patch. The two branches are then integrated through a feature-wise linear modulation mechanism. This framework provides a flexible design that allows different CNN architectures to be paired as the two branches. In this way, the model leverages informative neighbourhood context while reducing redundancy and prioritises features most predictive of the class label.

2 Study area and data

2.1 Study area description

Nantou County is located in the central part of Taiwan and forms a key section of the islandôs mountain range (Fig. 1a). The topography varies greatly, with elevations ranging from about 20 m in the western lowlands, which are mainly occupied by built-up areas, to approximately 3800 m in the eastern mountains characterised by steep slopes and complex geological formations. According to the Kº ppen climate classification [51], Nantou falls within the humid subtropical climate zone (Cfa), strongly influenced by the East Asian monsoon. Precipitation varies considerably due to the blocking effect of the mountainous terrain on moisture-laden air masses, with annual averages of around 1750 mm in the western plains and more than 2800 mm in the eastern mountains [52]. Most rainfall occurs between April and September during the monsoon season. The geological and climatic conditions make Nantou highly susceptible to landslides, making it an important and representative site for landslide-related research [53,54]. In this study, Jenai and Sinyi Townships, located in the eastern part of Nantou County and covering a combined area of about 2,644 kmĮ, were selected as the study area (Fig. 1b). To further examine whether the effectiveness of the proposed LGSCF framework can be reproduced beyond the primary study area, Hualien County in eastern Taiwan was additionally selected for cross-regional validation. Despite their geographical proximity, Nantou and Hualien differ in their environmental settings, with Nantou characterised by an inland mountainous landscape and Hualien by an eastern coastal setting, leading to differences in terrain and rainfall regimes.

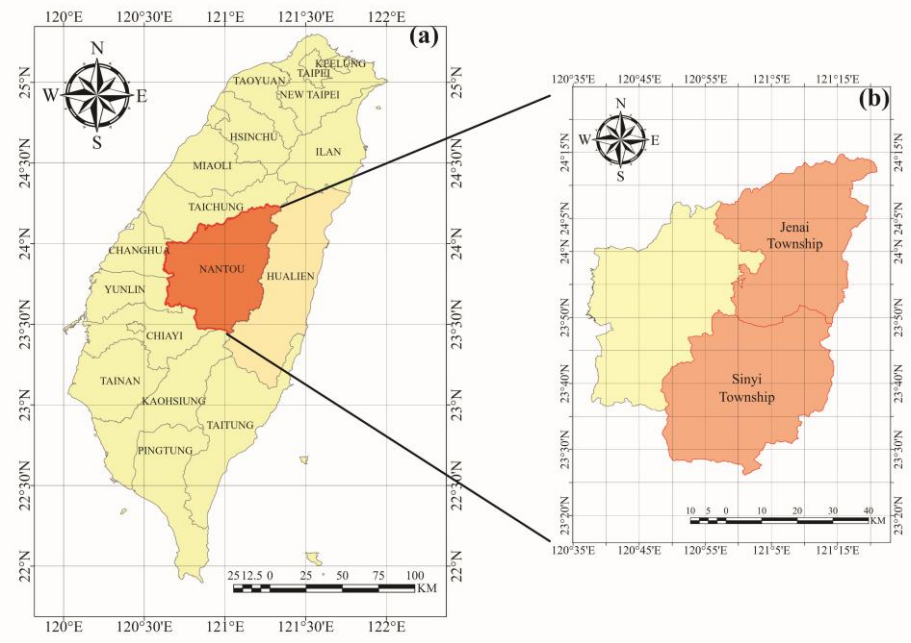

Fig. 1. Location of (a) Nantou County and Hualien County in Taiwan and (b) the primary study area

comprising Jenai and Sinyi Townships in eastern Nantou County.

2.2 Landslide inventory

The accuracy of landslide points is critical for reliable landslide susceptibility analysis [55]. In this study, the landslide inventory was derived from the 2022 Annual Landslide Inventory Map of Taiwan [56]. The map was produced through visual interpretation of SPOT satellite imagery with a minimum mapping unit of 0.1 hectares. Crown areas are commonly used as representative points in landslide susceptibility analysis [57]. In this study, 5332 landslide points were extracted within the study area (Fig. 2).

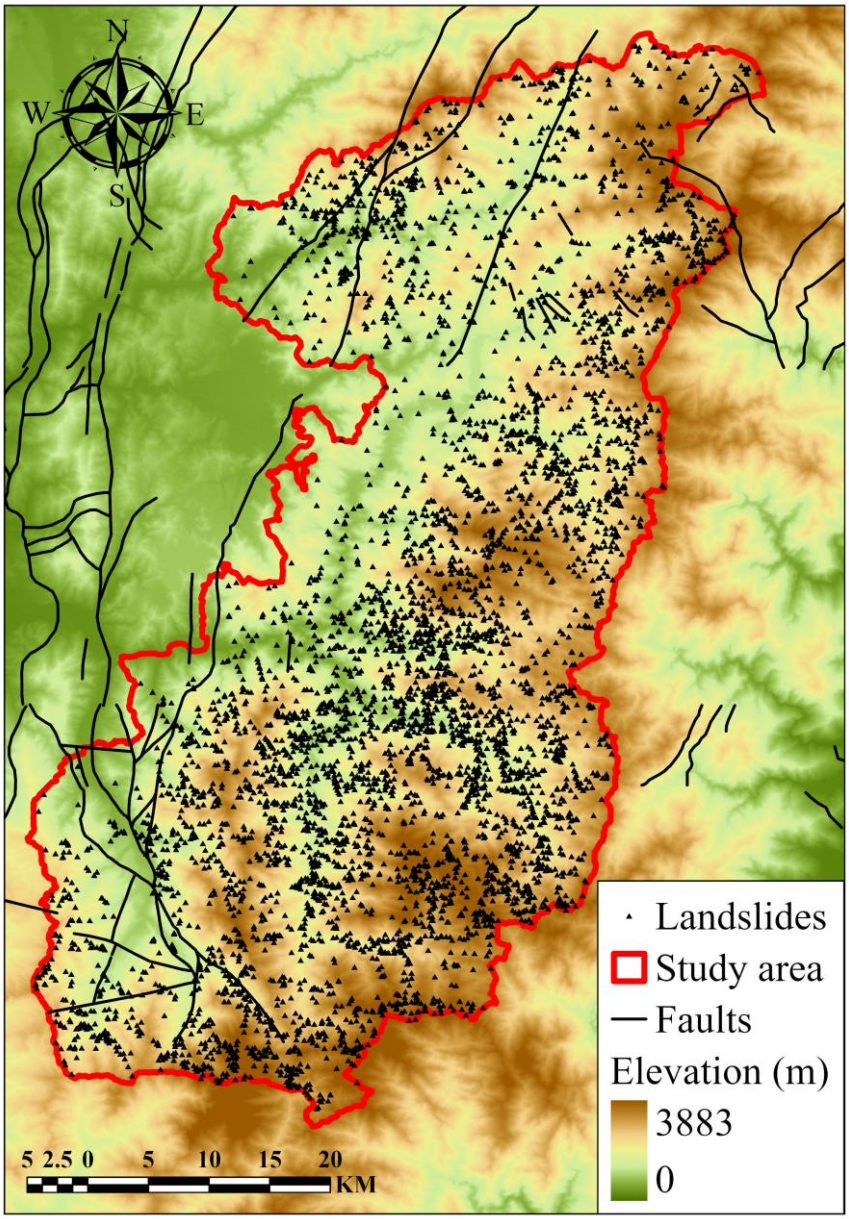

Fig. 2. Spatial distribution of the 5332 landslide inventory points within the study area.

2.3 Landslide geo-environmental conditioning factors (LCFs)

Data-driven LSM estimates the likelihood of landslide occurrence by learning the relationships between observed landslides and their geo-environmental settings. The selection of appropriate LCFs is therefore a critical step. Although numerous LCFs have been used in previous studies, no universally accepted selection method exists because their relevance depends on the landslide type, spatial scale, regional setting, and data availability [58ï 61]. In this study, fifteen LCFs were selected to represent five groups of landslide controls: topographic, geological, hydrological, surface environmental, and human-related factors. The selection was guided by their established use in regional LSM, their physical relevance to landslide occurrence, and the availability of datasets with consistent coverage across Nantou County. These factors are particularly relevant to the steep terrain, complex geological setting, monsoon-dominated rainfall, variable land cover, and road development that characterise Nantou County [52ï 54].

Other potentially relevant factors were considered but not included in the present analysis. Soil type was excluded because a region-wide dataset with spatial resolution and attribute consistency comparable to other inputs was unavailable. Lithology and LULC were therefore retained to characterise surface conditions, although they cannot fully substitute for detailed soil information. Landform classes were not included as separate inputs because they are commonly derived from DEM-based terrain attributes already represented by elevation, slope, aspect, curvature, TRI, TWI, and SPI. Plane and profile curvature were included among the fifteen LCFs, whereas additional curvature derivatives were omitted to avoid introducing closely related terrain variables. Seismicity was also excluded because this study addresses general landslide susceptibility rather than an event-specific coseismic scenario. A meaningful seismic predictor, such as peak ground acceleration, would require spatial ground-motion data temporally matched to the landslide inventory [62ï 64].

All LCFs were processed into raster format and resampled to a uniform spatial resolution of 30 m Ĭ 30 m to ensure consistency in subsequent modelling. The details and spatial distributions of these LCFs are presented in Table 1 and Fig. 3.

Table 1. Data sources for LCFs used in this study

Data	Sources	LCFs
DEM	ASTER Global Digital Elevation Model (GDEM) V003 (30m)	elevation, slope, aspect, plane curvature, profile curvature, stream power index, TWI, and topographic roughness index.
lithology	Derived from the ñTaiwan National	Lithology

fault lines	Land Surveying and Mapping Information Web Map Serviceòand manually vectorised	Distance to faults
NDVI	Chinese Academy of Science Discipline Data Centre for Ecosystem (30m) [65]	NDVI
LULC	The global 2000-2020 LULC dataset (30m) [66]	LULC
rainfall	CMORPH Climate Data Record (CDR), resampled to 30m	rainfall
road networks	OpenStreetMap	Distance to roads
river networks		Distance to rivers

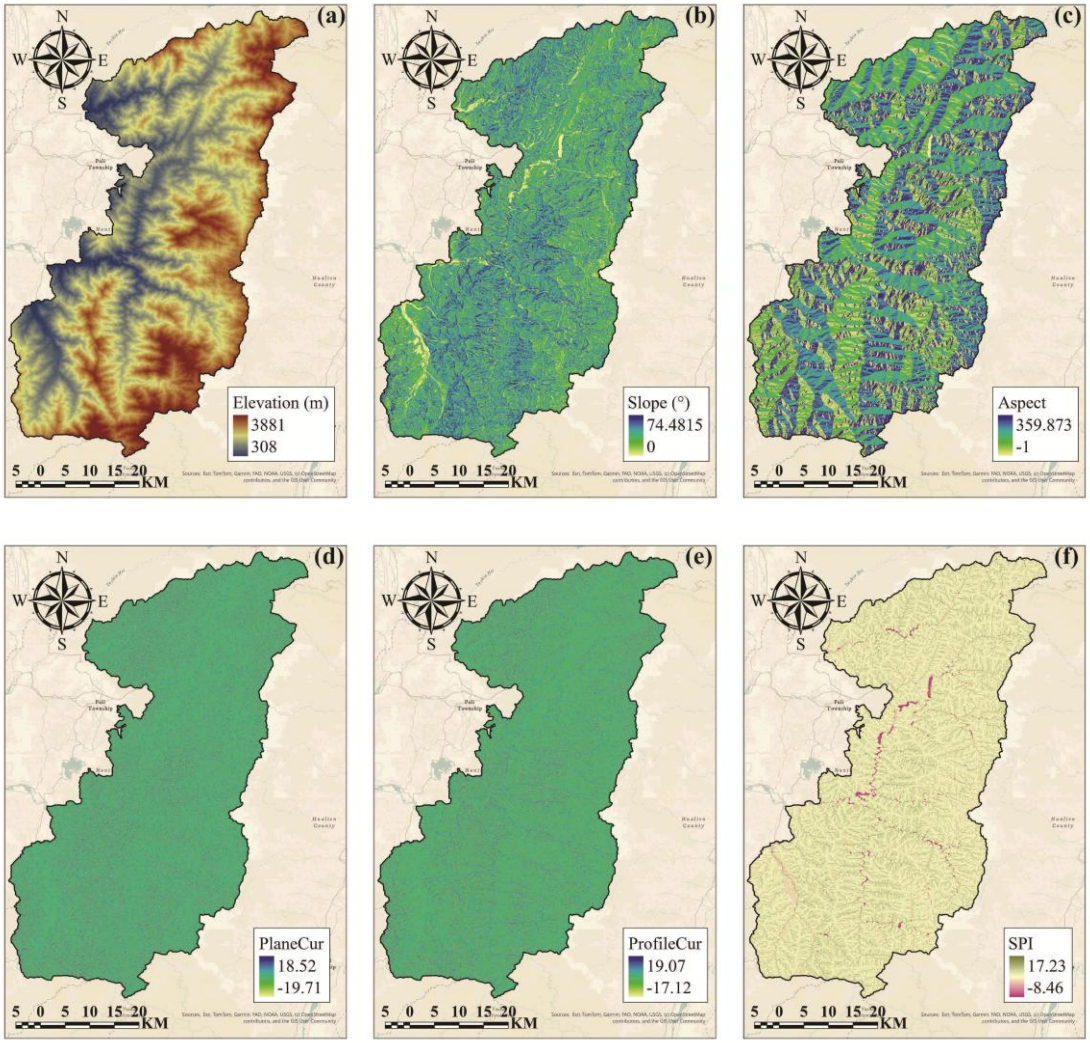

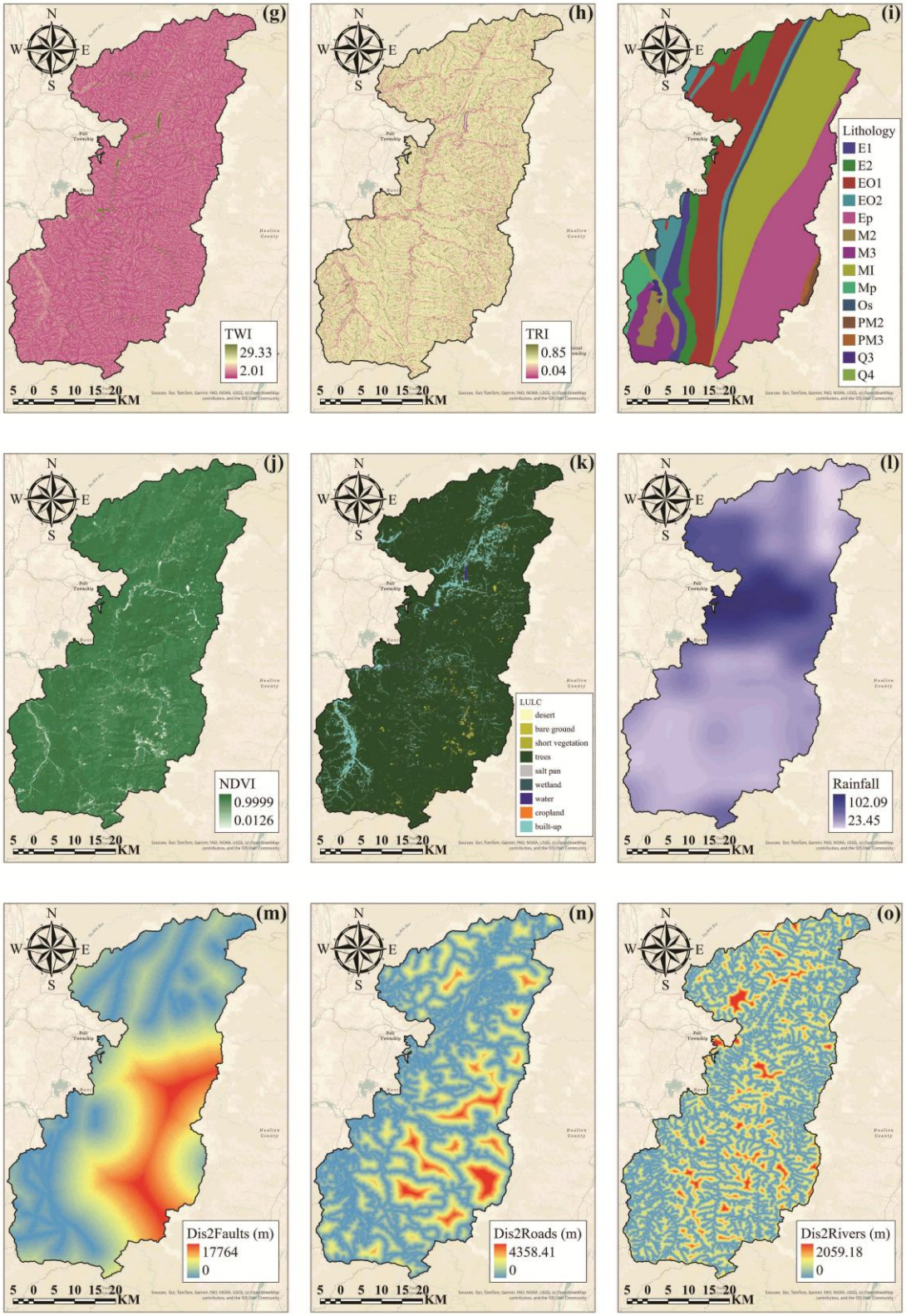

Fig. 3. Spatial distributions of the 15 LCFs used in this study: (a) elevation; (b) slope; (c) aspect; (d) plane curvature; (e) profile curvature; (f) SPI; (g) TWI; (h) TRI; (i) lithology; (j) NDVI; (k) LULC; (l) rainfall; (m) distance to faults; (n) distance to roads; (o) distance to rivers.

3 Methodology

3.1 LCFs multicollinearity diagnostics

Reliable landslide susceptibility modelling requires that the input LCFs do not exhibit strong linear dependency, as strongly correlated LCFs may obscure the individual contribution of each factor and affect model stability. To address this, we employed two commonly used multicollinearity diagnostic measures: tolerance (TOL) and the variance inflation factor (VIF), as shown in Formula (1).

$$VIF = \frac{1}{1 - R^2} = \frac{1}{TOL} \tag{1}$$

where *RĮ* is the coefficient of determination obtained by regressing one factor against all others, and *VIF* is the reciprocal of *TOL,* which quantifies how much the variance of a regression coefficient is inflated due to correlation among factors.

In general, TOL values lower than 0.1 and VIF values greater than 10 are regarded as the existence of multicollinearity.

3.2 Dataset construction

Data-driven landslide susceptibility modelling is essentially a binary classification task, which requires both landslide points (positive samples) and non-landslide points (negative samples). A variety of strategies for selecting non-landslide points have been proposed and applied in previous studies [67ï 69]. In this study, the frequency ratio (FR) model was adopted to select non-landslide samples [70ï 72]. The FR-based sampling strategy was intended to reduce the risk of treating unrecorded or potentially unstable locations as non-landslide samples, because the absence of an inventory record does not necessarily confirm slope stability.

The FR method is a statistical approach that measures the relationship between the spatial distribution of landslides and the corresponding classes of LCFs. FR values were calculated using Formula (2) and then normalised to relative frequency (RF), as shown in Formula (3). Based on these results, the prediction rate (PR) was derived according to Formula (4). To minimise the likelihood of mislabelling unstable areas as negative samples, the product of each factorŝ PR and the RF of its classes was calculated, and non-landslide samples were randomly selected from the very low susceptibility zones to match the number of landslide samples.

$$FR_{ij} = \frac{LA_{ij} \big/ LA_t}{A_{ij} \big/ A_t} \tag{2}$$

$$RF_{ij} = \frac{FR_{ij}}{\sum_{k=1}^{m_i} FR_{ik}} \tag{3}$$

$$PR_i = \frac{(RF_{i,max} - RF_{i,min})}{min_{r=1,2,\ldots,n}(RF_{r,max} - RF_{r,min})} \tag{4}$$

where i denotes the i-th LCF and j denotes its j-th category. LA_{ij} and A_{ij} represent the landslide area and the total area within category j of LCF i, respectively, while LA_t and A_t are the total landslide area and the total area of the study area. FR_{ij} is the frequency ratio of category j within LCF i. A value greater than 1 indicates that landslides are proportionally more concentrated in that category than in the study area as a whole. In Equation (3), m_i is the number of categories within LCF i, and RF_{ij} is the normalised relative frequency, for which the values of all categories within the same LCF sum to 1. In Equation (4), $RF_{i,\max}$ and $RF_{i,\min}$ are the maximum and minimum RF values among the categories of LCF i, respectively; n is the total number of LCFs; and r indexes the LCFs. PR_i is the prediction rate of LCF i, obtained by normalising its RF range against the smallest RF range among all LCFs.

To ensure class balance, an equal number of non-landslide points (5332) were selected to match the landslide points. The selected landslide and non-landslide points were organised into image patches to construct the dataset. A previous study has shown that the side length of image patches can influence modelling performance, and patch sizes that approximate the average landslide size within the study area tend to yield better results [73]. In our study, the average landslide area is approximately 16333.7 mĮ, corresponding to a side length of about 127.8 m. Given the resolution of 30 m, an 11Ĭ 11 image sample was generated by extending five pixels outward in all directions from each selected point (either landslide or non-landslide). This sample size was chosen to ensure adequate coverage of the typical landslide extent while maintaining a manageable input size for the following modelling procedure. Combined with the 15 LCFs, each image patch sample thus has a structure of 11Ĭ 11Ĭ 15. The dataset was then divided into training and validation sets in a 7:3 ratio.

3.3 Modelling description

To address the limitations of previous methods stated in Section 1, this study proposes the LGSCF strategy for landslide susceptibility mapping, based on a dual-branch CNN design (Fig. 4). The input sample is denoted as $X \in \mathbb{R}^{11\times11\times15}$. The spatial-context branch takes the full patch X as input and is designed to capture both the landslide or non-landslide characteristics and the surrounding contextual patterns. After convolutional processing, the spatial-context branch outputs a one-dimensional feature vector $s \in \mathbb{R}^k$. In parallel, the local-geo branch encodes a 15-dimensional vector consisting of the LCF values of the centre pixel, which corresponds to either a landslide or non-landslide

location, denoted as $X_c \in \mathbb{R}^{15}$. After 1D convolution, the local-geo branch yields a feature representation $c \in \mathbb{R}^{D_c}$.

Regarding feature fusion, a straightforward approach would be concatenation. However, this design faces two potential issues. First, as the spatial-context branch inherently includes the centre pixel information, direct concatenation with the local-geo branch may introduce feature redundancy. Second, the two branches process inputs of different dimensionality and semantic scope (patch-level vs pixel-level), so direct concatenation could result in inconsistency in physical meaning. Therefore, in this study, we draw inspiration from Feature-wise Linear Modulation (FiLM) [74,75]. The core idea of FiLM is to condition one feature representation on another by generating feature-wise scaling and shifting parameters. In this study, specifically, the local-geo representation c is transformed into modulation parameters $\gamma, \beta \in \mathbb{R}^k$ through a two-layer multilayer perceptron (MLP) (Formula 5), which are then used to perform feature-wise affine modulation of the spatial representation s (Formula 6).

$$[\gamma, \beta] = g(c; \theta_g) \in \mathbb{R}^{2k} \tag{5}$$

where θ_g denotes the learnable parameters of the MLP.

$$f = \gamma \odot s + \beta \tag{6}$$

where $\odot$ denotes feature-wise multiplication. The fused vector f is subsequently fed into fully connected layers for final classification.

Conceptually, LGSCF is an intermediate feature-level fusion strategy rather than a generic multimodal learning paradigm. It differs from conventional attention-based fusion, in which channel, spatial, or token attention generally derives weights over feature channels, spatial locations, or token-to-token interactions. LGSCF does not construct an attention map or calculate similarity between feature tokens. Instead, it performs cross-branch affine modulation, in which the local-geo representation generates both multiplicative and additive parameters for the spatial-context features. The scaling operation strengthens or suppresses individual contextual responses, while the additive shift allows the conditioned representation to move beyond simple multiplicative reweighting. This mechanism is particularly relevant to LSM because the class label corresponds to a specific central location, whereas the surrounding patch may contain informative or unrelated terrain patterns. The relevance of this contextual information depends on the geo-environmental conditions at the target location. For instance, similar neighbourhood patterns may have different implications under different topographic, geological, or hydrological settings. LGSCF therefore uses the central-location characteristics to guide how the surrounding context is interpreted, providing a task-specific form of directional conditioning.

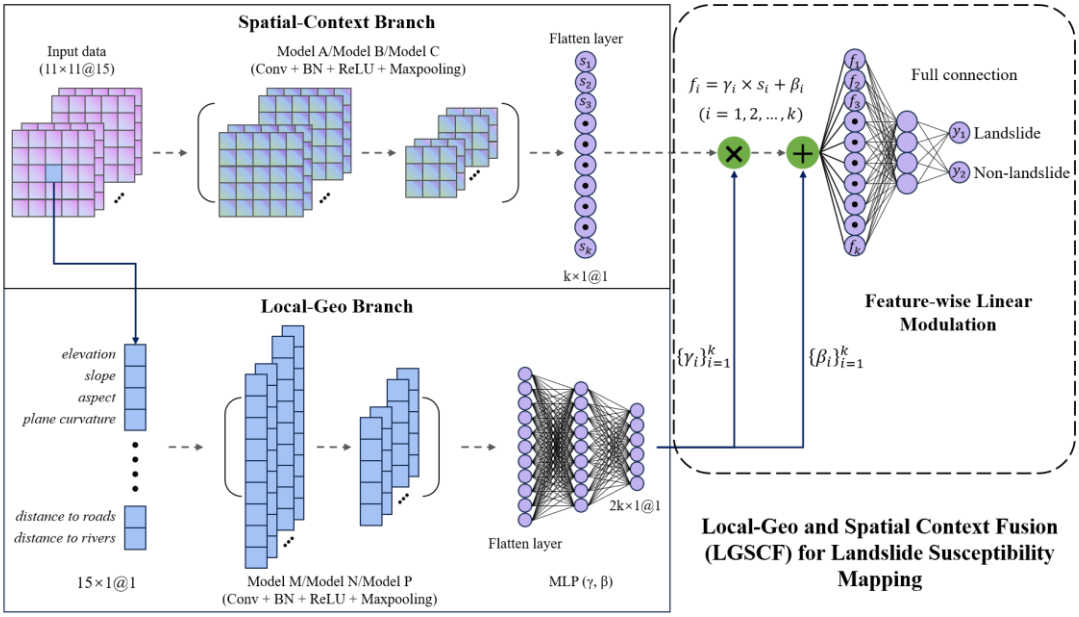

Fig. 4. Architecture of the proposed LGSCF strategy. Models A, B, and C represent the spatial-context branch, while Models M, N, and P correspond to the local-geo branch. Further details are provided in Table 3.

To evaluate the effectiveness of the proposed LGSCF strategy, we selected six representative baseline CNN architectures, including three spatial-context branch models (denoted as Models A, B, and C) and three local-geo branch models (denoted as Models M, N, and P). Details of these baseline models are summarised in Table 3. By combining each model for the spatial-context branch with that for the local-geo branch in turn, nine LGSCF-based models were constructed for comparison, as listed in Table 4. Combinations within the same branch type (for example, two spatial-context branches or two local-geo branches) were not considered, as they cannot provide complementary information and thus hold little practical meaning. In all cases, the fully connected layers of the baseline models were removed, and outputs up to the flatten layer were retained to enable feature-level fusion.

Table 3. Baseline models used in this study.

Model ID	References	Main architectural characteristics	Branch type
Model A	[32]	3D convolution-based feature extraction.	Spatial-context branch
Model B	[76]	CNN with sequential channel and spatial attention (CBAM).	
Model C	[77]	CNN component adapted from a physically-based probabilistic model with CNN (PPM-CNN) framework.	
Model M	[32]	1D convolution-based feature extraction.	Local-geo branch
Model N	[37]	1D CNN with hierarchical convolution and pooling.	

Model P	[38]	CNN component adapted from the CNN and deep forest (CNN-DF) framework.

Table 4. List of LGSCF-based models and their corresponding baselines.

Model ID	Model M	Model N	Model P
Model A	Model A+M	Model A+N	Model A+P
Model B	Model B+M	Model B+N	Model B+P
Model C	Model C+M	Model C+N	Model C+P

Notes: Models A, B, and C represent the spatial-context branch, while Models M, N, and P correspond to the local-geo branch, as detailed in Table 3. Combinations within the same branch type are not applicable to the proposed LGSCF strategy.

Hyperparameter optimisation was conducted independently for each baseline and LGSCF-based model using an exhaustive grid search over batch size and initial learning rate (Table 5). Two batch sizes (32 and 64) and five initial learning rates (10^{-5}, 10^{-4}, 10^{-3}, 10^{-2}, 10^{-1}) were considered, resulting in ten candidate configurations for each model. To reduce the influence of random weight initialisation and data shuffling, each configuration was independently trained eight times using random seeds from 0 to 7. All candidate configurations used the Adam optimiser, cross-entropy loss, and a polynomial learning-rate scheduler with a decay power of 0.9. Training was limited to 200 epochs, with early stopping applied when the validation loss failed to improve by more than 1×10^{-4} for ten consecutive epochs. For each model, the candidate configurations were ranked according to their mean validation AUC across the eight runs, and the configuration with the highest mean AUC was selected for subsequent evaluation. Using the mean performance rather than the best individual run reduced the likelihood of selecting a configuration based on a favourable random initialisation. All other training settings were kept unchanged to ensure a consistent comparison among models.

Table 5. Training configurations of baseline models and LGSCF-based models.

Settings	Values
Batch sizes	32, 64
Initial learning rates	10^{-5}, 10^{-4}, 10^{-3}, 10^{-2}, 10^{-1}
Learning rate scheduler	Polynomial decay (PolyLR), with decay power $p = 0.9$
Optimizer	Adam
Loss function	Cross-entropy
Number of epochs	200
Early stopping	Monitored on validation loss, with tolerance 1Ĭ 10^{i4} and patience of 10 epochs.
Random seeds	For each setting, training was repeated with 8 seeds (0ï 7) to reduce variance and report stable statistics.

3.4 Accuracy assessment strategy

Accurate evaluation is essential to measure the reliability and performance of data-driven models in LSM. In this study, all evaluations were computed on the validation set. Several complementary metrics commonly used in classification tasks are employed. These metrics are derived from the confusion matrix (Fig. 5), which consists of true positives (TP, correctly identified landslides), true negatives (TN, correctly identified non-landslides), false positives (FP, non-landslides incorrectly identified as landslides), and false negatives (FN, landslides incorrectly identified as non-landslides). Based on these quantities, overall accuracy is defined as the proportion of correctly classified samples among all samples. Precision measures the fraction of correctly predicted landslides among all predicted landslides, while recall measures the fraction of actual landslides that are correctly detected. The F1 score, defined as the harmonic mean of precision and recall, accounts for both FP and FN and provides an overall indicator of classification effectiveness.

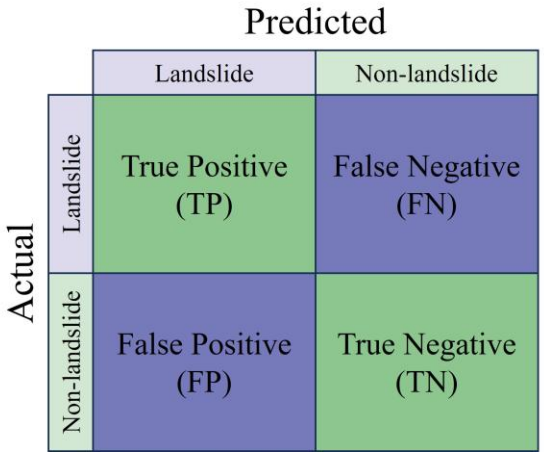

$$Accuracy = \frac{TP + TN}{TP + TN + FP + FN}$$

$$Precision = \frac{TP}{TP + FP}$$

$$Recall/Sensitivity = \frac{TP}{TP + FN}$$

$$F1 - score = \frac{2 \times Precision \times Recall}{Precision + Recall}$$

Fig. 5. Binary confusion matrix and equations used to calculate accuracy, precision, recall (sensitivity), and F1-score.

In addition to the confusion matrix, the receiver operating characteristic (ROC) curve is also a commonly used and reliable tool for evaluating model performance in LSM [78ï 80]. The ROC curve plots the true positive rate (TPR) against the false positive rate (FPR) at different decision thresholds, providing an overall view of classification ability. The area under the ROC curve (AUC) is a quantitative measure derived from the ROC curve. An AUC value closer to 1 indicates stronger discriminative power, while a value near 0.5 suggests performance comparable to random guessing.

Beyond classification metrics, Root Mean Squared Error (RMSE) and Mean Absolute Error (MAE) were further used to assess the numerical consistency between predicted susceptibility values and reference labels. RMSE penalises larger errors more heavily (Formula 7), while MAE reflects the average magnitude of errors. Lower values indicate more accurate susceptibility predictions (Formula 8).

$$RMSE = \sqrt{\frac{\sum_{i=1}^{M}(y_i - y_i')^2}{M}} \tag{7}$$

$$MAE = \frac{\sum_{i=1}^{M}|y_i - y_i'|}{M} \tag{8}$$

where *M* is the total number of samples used for the evaluation. y_i denotes the actual value for the *i*-th sample, while y_i' denotes the predicted value for the *i*-th sample.

3.5 Model interpretation using SHAP

SHapley Additive exPlanations (SHAP) was used to interpret the contribution of each LCF to model predictions. SHAP is an additive feature-attribution method derived from the Shapley value in cooperative game theory [1,2]. It treats the input features as players and measures the contribution of each feature by considering its marginal effect across all possible feature combinations. For a sample x, the SHAP value of feature i is calculated as:

$$\phi_i(x) = \sum_{S \subseteq F \setminus \{i\}} \frac{|S|!(M-|S|-1)!}{M!}[v_x(S \cup \{i\}) - v_x(S)] \tag{9}$$

where F is the complete set of M input features, S is a subset of features not containing feature i, and $v_x(S)$ denotes the expected model output when only the features in S are known. The weighting term accounts for all possible orders in which feature i can be added to a feature combination. The model prediction can then be expressed as:

$$f(x) = \phi_0 + \sum_{i=1}^{M} \phi_i(x) \tag{10}$$

where $\phi_0 = E[f(X)]$ is the expected model output and $\phi_i(x)$ represents the contribution of feature i to the prediction.

A positive SHAP value indicates that the feature increases the predicted landslide susceptibility relative to the expected output, whereas a negative value indicates the opposite. Local SHAP values explain individual predictions, while global feature importance was evaluated by averaging the absolute SHAP values of each feature across all samples.

4 Results

4.1 Results of LCFs multicollinearity diagnostics

As shown in Fig. 6, the TOL values of the 15 selected LCFs ranged from 0.487 to 0.953, with the highest value observed for aspect (0.953) and the lowest for plane curvature (0.487). Correspondingly, the VIF values ranged from

1.049 to 2.053, with aspect exhibiting the lowest VIF (1.049) and plane curvature the highest (2.053). The VIF values were all below the commonly used threshold of 10, and all TOL values exceeded 0.1. The results indicated that the multicollinearity among the LCFs was insignificant, and all LCFs were therefore suitable for subsequent susceptibility analysis.

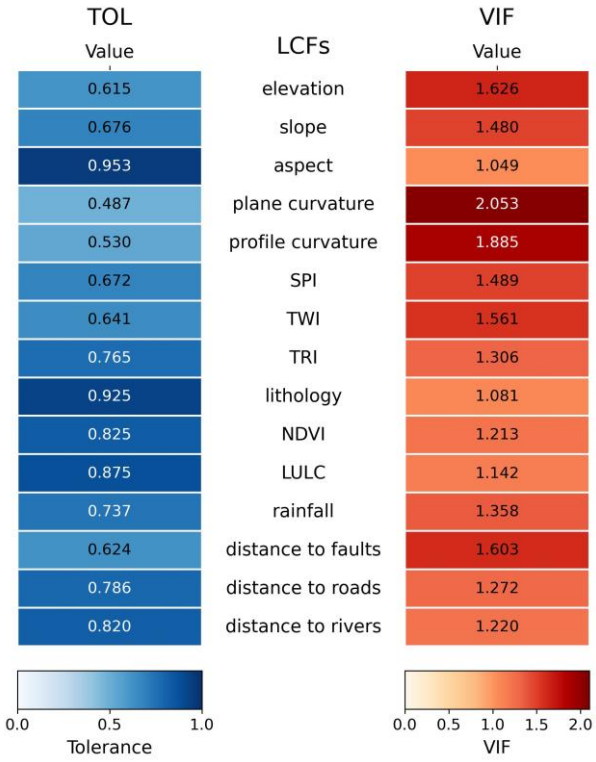

Fig. 6. Multicollinearity diagnostics (TOL and VIF) for the LCFs used in this study.

4.2 Configurations of best-performing models

As illustrated in Table 5, various batch sizes and learning rates were explored during model training to ensure a fair comparison across different architectures. Each configuration was run multiple times using random seeds. The mean AUC values were calculated and used to rank the configurations. Fig. 7 summarises the optimal settings corresponding to the best predictive performance for each model. The results show that a batch size of 32 consistently yielded competitive performance across most model variants, while a larger batch size of 64 was more frequently selected by the LGSCF-based models by enhancing gradient stability. Regarding the learning rate, most models achieved their best performance with values of 10^{-4} or 10^{-3}, while only a few models selected 10^{-2}, and none chose 10^{-5} or 10^{-1}.

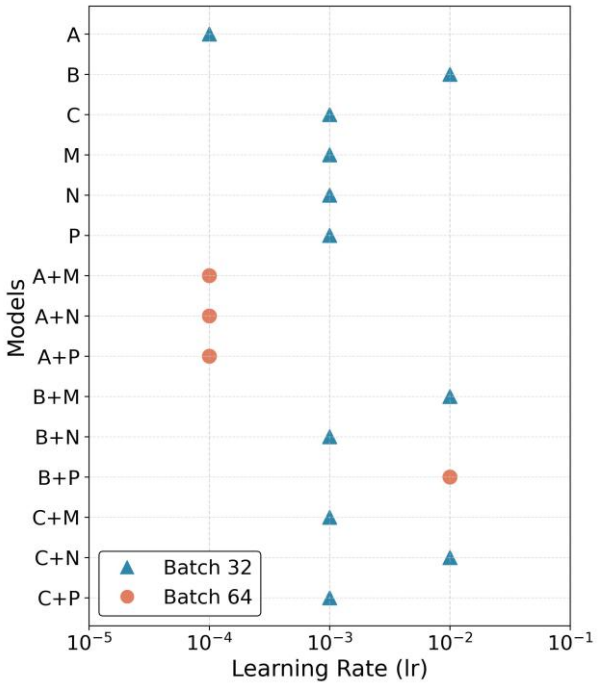

Fig. 7. Batch size and initial learning rate selected for each baseline and LGSCF-based model based on the highest mean validation AUC across eight repeated runs.

4.3 Susceptibility map of the study area.

To visualise the predictive results, we used the best-performing run to generate the landslide susceptibility map for each model. The outputs were classified into five susceptibility levels: "very low", "low", "moderate", "high", and "very high", using the geometric interval method [81,82]. Fig. 8 presents the susceptibility maps of Model A+M together with its two baselines, Models A and M, while the maps from other models are provided in Appendix A.

Overall, the three maps display broadly consistent spatial patterns: "very high" susceptibility zones were concentrated in the southeast, followed by the northeast, whereas the western region was dominated by "low" and "very low" susceptibility levels. This distribution aligns well with the topography and the actual landslide distribution, as the mountainous east is more prone to slope failures than the flatter west. Looking more closely, however, some differences can be noted in how the models delineated susceptibility levels. Within the "high" susceptibility areas, Model A+M still identified patches of "very low" susceptibility, while Models A and M tended to assign these zones as "moderate". Conversely, in "very low" susceptibility regions, Model A+M assigned more "moderate" zones, reflecting a more conservative classification behaviour.

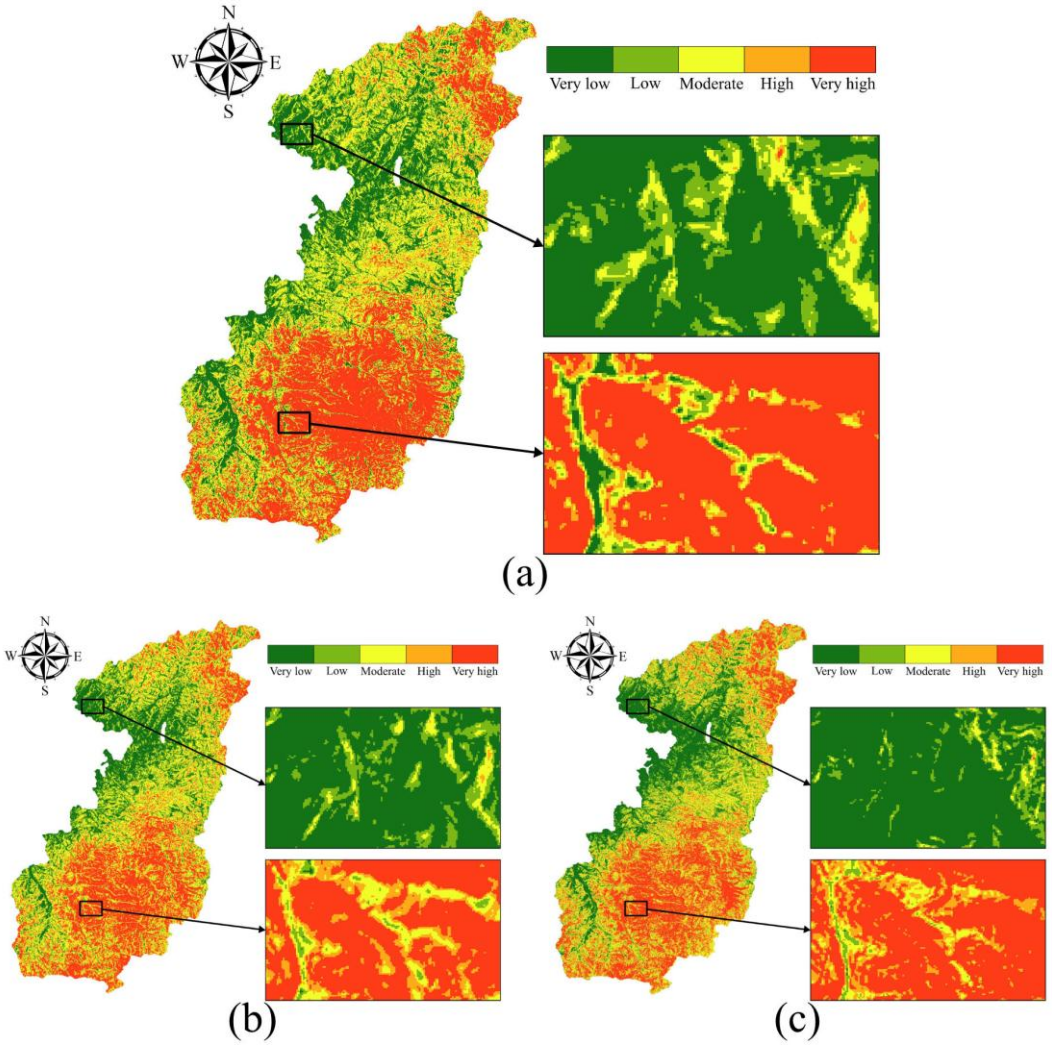

Fig. 8. Landslide susceptibility maps produced by (a) the LGSCF-based Model A+M, (b) Model A, (c) Model M.

4.4 Model performance analysis

4.4.1 Classification metrics and ROC-AUC results

The evaluation metrics of the best-performing configuration were averaged across its runs (Table 6). For ROC curves, which cannot be directly averaged across runs, the curve corresponding to the median AUC run was selected for plotting (Fig. 9).

Among the baseline models, the spatial-context branch networks (Models A, B, and C) consistently outperformed the local-geo branch networks (Models M, N, and P). In particular, Models B and C achieved the strongest performance, with accuracy and F1-scores exceeding 86% and AUC values above 0.945. By contrast, the pixel-based models, especially Models M and N, achieved relatively weaker overall performance. Although their precision values were relatively high (above 88%), their recall dropped below 78%, suggesting that these models tended to overemphasise one class and failed to provide

balanced predictions across positive and negative samples.

When comparing the LGSCF-based models with their baselines, a clear and consistent improvement can be observed (Table 6). The F1-score and AUC are consistently higher for the LGSCF-based models than for their corresponding baselines, with the gains particularly evident for the weaker local-geo (Models M, N, and P). Even for the stronger spatial baselines (Models A, B, and C), the LGSCF-based models still achieved marginal but steady improvements. For example, Models B+N and C+P achieved AUC values of 0.9473 and 0.9472, respectively, both higher than their already strong baselines. This demonstrates that synergising local geo-environmental information with spatial context provides a complementary effect that enhances overall predictive performance. It not only compensates for weaker baselines but also further refines strong ones, highlighting the broad applicability of the LGSCF strategy. The ROC curves (Fig. 9) further confirm these findings, as the LGSCF-based models lifted the curves upward across most of the false positive rate range. Nevertheless, precision and recall still varied in some cases, indicating that the balance between detecting positives and negatives was not yet perfect. Even so, compared with the pixel-based baselines, the LGSCF-based models achieved a much more acceptable balance, approaching that of the spatial baselines. This also suggests that the characteristics of the two branch types exerted a potential influence on the performance of the LGSCF-based models.

Table 6. Averaged evaluation metrics of baseline and LGSCF-based models from the best-performing configuration (based on mean AUC value).

Types	Models	Accuracy	Precision	Recall	F1-score	AUC
Spatial-context branch CNNs	A	84.018%	85.638%	82.298%	83.827%	0.92043
	B	86.858%	89.516%	84.186%	86.577%	0.94506
	C	86.224%	86.887%	86.193%	86.317%	0.94537
Local-geo branch CNNs	M	83.633%	87.969%	78.354%	82.805%	0.91515
	N	83.452%	88.129%	77.741%	82.537%	0.91484
	P	83.657%	90.514%	75.518%	82.297%	0.92001
LGSCF-based CNNs	A+M	84.539%	88.809%	79.892%	83.843%	0.92716
	A+N	84.223%	85.066%	83.636%	84.222%	0.92510
	A+P	84.572%	87.798%	80.792%	84.052%	0.92621
	B+M	87.255%	90.193%	84.003%	86.905%	0.94720
	B+N	87.416%	90.271%	84.114%	87.063%	0.94640
	B+P	87.055%	87.764%	86.632%	87.089%	0.94662
	C+M	86.978%	87.816%	86.265%	86.951%	0.94604
	C+N	87.311%	89.864%	84.528%	86.996%	0.94668
	C+P	87.131%	88.239%	86.058%	87.073%	0.94694

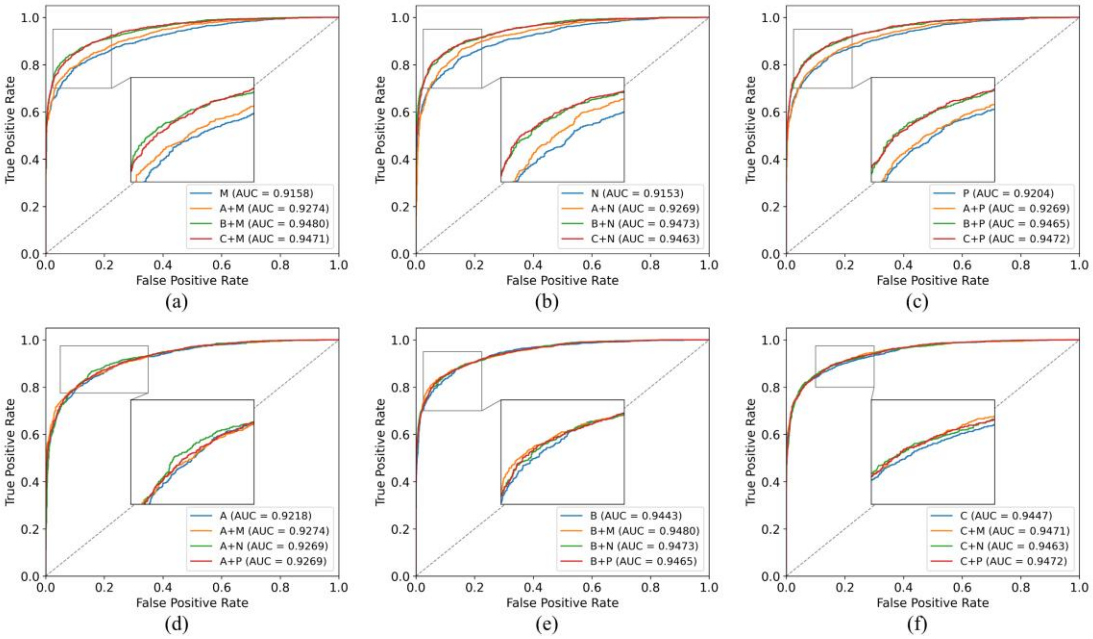

Fig. 9. ROC curves of baseline models and their LGSCF-based combinations: (a) Model M, (b) Model N, (c) Model P, (d) Model A, (e) Model B, (f) Model C. Further details of the base models and their LGSCF-based combinations are provided in Tables 3 and 4.

4.4.2 Error-based evaluation (RMSE and MAE)

Fig. 10 compares the RMSE and MAE of the baseline models and their corresponding LGSCF-enhanced variants. Overall, incorporating additional branches consistently reduced prediction errors relative to the single-branch baselines, indicating the effectiveness of the LGSCF strategy. Among the spatial-context branch models (Models A, B, and C), Model B achieved the most noticeable reductions in both RMSE and MAE, while improvements for Models A and C were more moderate. For the local-geo branch models (Models M, N, and P), the performance gains were particularly pronounced. This trend is consistent with the ROCï AUC results, indicating agreement between classification- and error-based evaluation strategies.

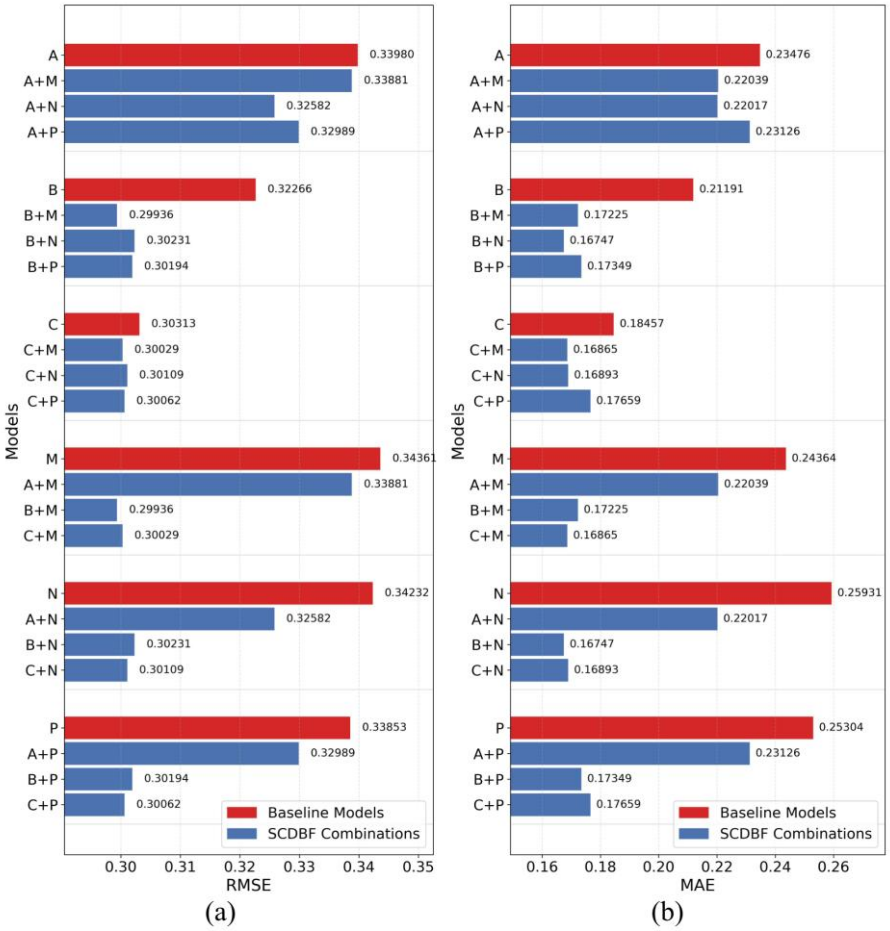

Fig. 10. RMSE and MAE of baseline models and their corresponding LGSCF-based combinations: (a) RMSE, (b) MAE.

4.5 Analysis of the Importance of Factors

Fig. 11 presents the SHAP interpretations of Models B, M, and B+M. In the beeswarm plots, each point represents an individual sample, while the feature-importance plots rank the LCFs according to their mean absolute SHAP values. Despite differences in their relative rankings, distance to faults, DEM, distance to rivers, slope, and rainfall consistently formed the dominant factor group across all three models. Model B placed greater emphasis on distance to faults, DEM, and distance to rivers (Fig. 11a,b), whereas Model M was driven more strongly by slope and rainfall (Fig. 11c,d). Following LGSCF fusion, Model B+M retained distance to faults as the leading factor while increasing the relative contributions of slope and rainfall (Fig. 11e,f). Thus, LGSCF did not introduce a different set of dominant factors but redistributed the contributions of the same core LCFs captured by the two branches. These factors collectively represent structural, topographic, and hydro-environmental controls, although their SHAP importance should not be interpreted as direct causality. DEM, for example, may act as a proxy for geomorphic position and the broader rainfallï erosion setting because it is associated with slope development, terrain dissection, orographic rainfall, and topographic energy. Similarly, distance to faults and

rivers may represent the spatial influence of structural weakening and fluvial incision rather than isolated distance effects. Curvature-related factors, NDVI, geology, and TRI made comparatively limited contributions, suggesting that their predictive information was either secondary or partly represented by the dominant factors.

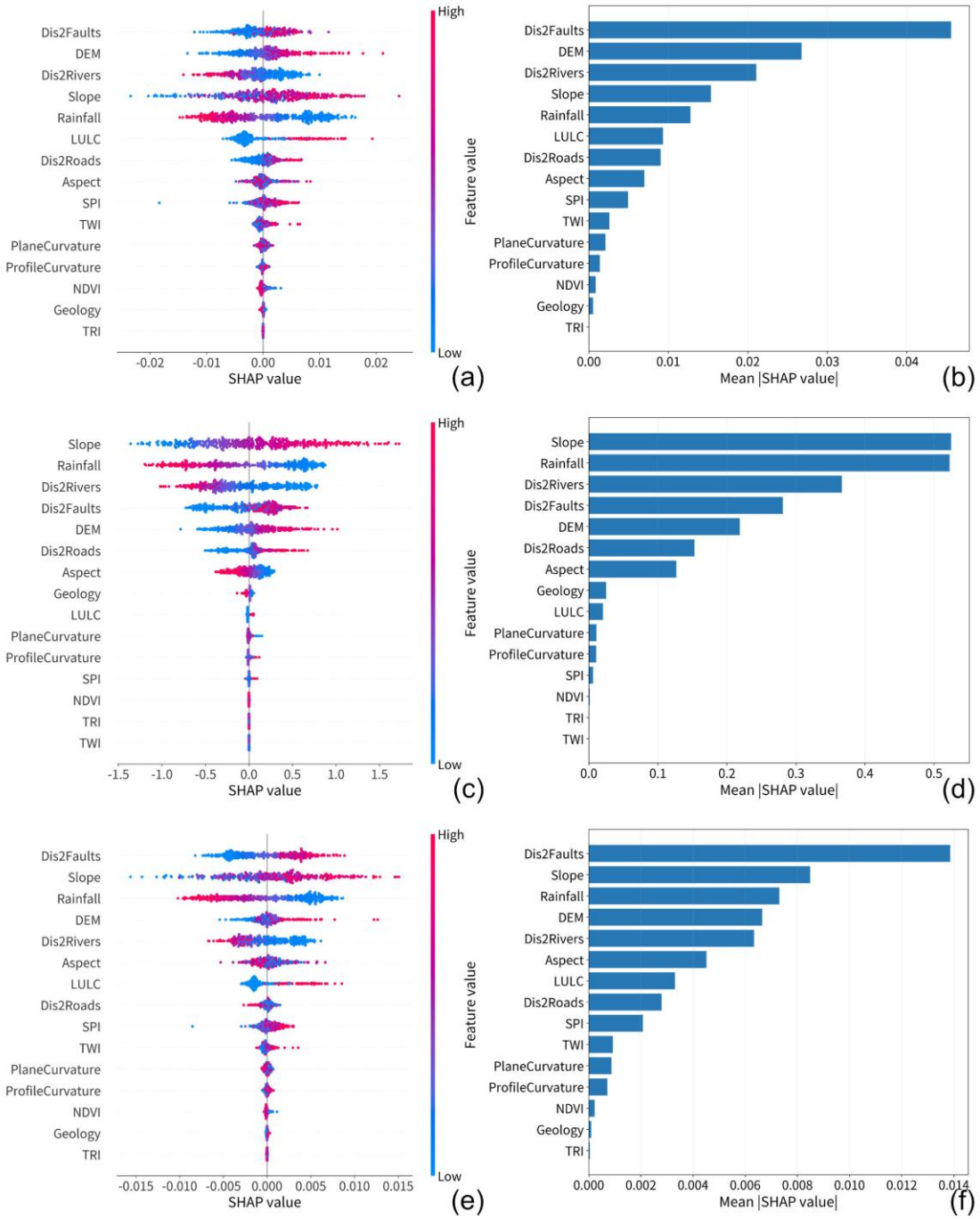

Fig. 11. SHAP-based interpretation of Models B, M, and B+M using beeswarm and mean absolute SHAP feature-importance plots: **(a)** and **(b)**: Model B; **(c)** and **(d)**: Model M; **(e)** and **(f)**: Model B+M.

5 Discussions

5.1 Comparison of landslide susceptibility maps

To further quantify how landslides are distributed across susceptibility levels, we calculated their percentages in each of the five classes (Table 7 and Fig. 12) and visualised the results for all baseline and LGSCF-based models. For the baseline models, around half of the landslides already fell in the "very high" susceptibility class, ranging from roughly 46% for Models M and N to over 55% for Models B and C. However, a considerable proportion was still scattered across the "moderate" and "high" classes, and some baselines allocated relatively large shares to the "low" and "very low" levels, particularly Models N, P, and B.

By contrast, the LGSCF-based models consistently increased the concentration of landslides in the "very high" class while reducing allocations to the lower susceptibility categories. For instance, Model A+M raised the proportion of "very high" susceptibility to 55.29%, compared with 52.76% and 45.91% for Models A and M, respectively. Similar improvements appeared across other combinations: Models B+M, B+N, and B+P all exceeded 59%, while Models C+N and C+P exceeded 62%. Model C+N reached the highest percentage of 66.84% in the "very high" susceptibility class, marking a clear improvement over both of its baselines. At the same time, the LGSCF-based models substantially reduced misclassifications in the lower categories. Whereas baseline models placed about 2% of landslides in the "very low" susceptibility class and, in some cases more than 10% in the "low" susceptibility class, the LGSCF-based models reduced the "very low" share to around 1%, while the combined total of "very low" and "low" is as small as roughly 5%.

Table 7. Percentage of landslides within each susceptibility class.

Models	Very low	Low	Moderate	High	Very high
Model A	1.44%	5.25%	19.49%	21.06%	52.76%
Model B	1.74%	14.10%	12.60%	15.92%	55.63%
Model C	2.44%	5.38%	20.35%	16.56%	55.27%
Model M	2.78%	9.49%	19.04%	22.79%	45.91%
Model N	3.56%	16.75%	15.98%	17.65%	46.06%
Model P	2.72%	10.17%	16.11%	16.79%	54.22%
Model A+M	1.43%	4.89%	21.94%	16.45%	55.29%
Model A+N	0.90%	5.14%	20.39%	14.72%	58.85%
Model A+P	1.24%	5.12%	20.56%	15.17%	57.91%
Model B+M	0.54%	3.71%	17.12%	13.99%	64.63%
Model B+N	0.81%	2.78%	19.56%	17.07%	59.79%
Model B+P	0.88%	3.30%	17.87%	13.99%	63.95%
Model C+M	1.09%	2.78%	18.14%	13.63%	64.37%

Model C+N	0.88%	2.81%	16.20%	13.26%	66.84%
Model C+P	1.09%	3.17%	18.19%	15.40%	62.15%

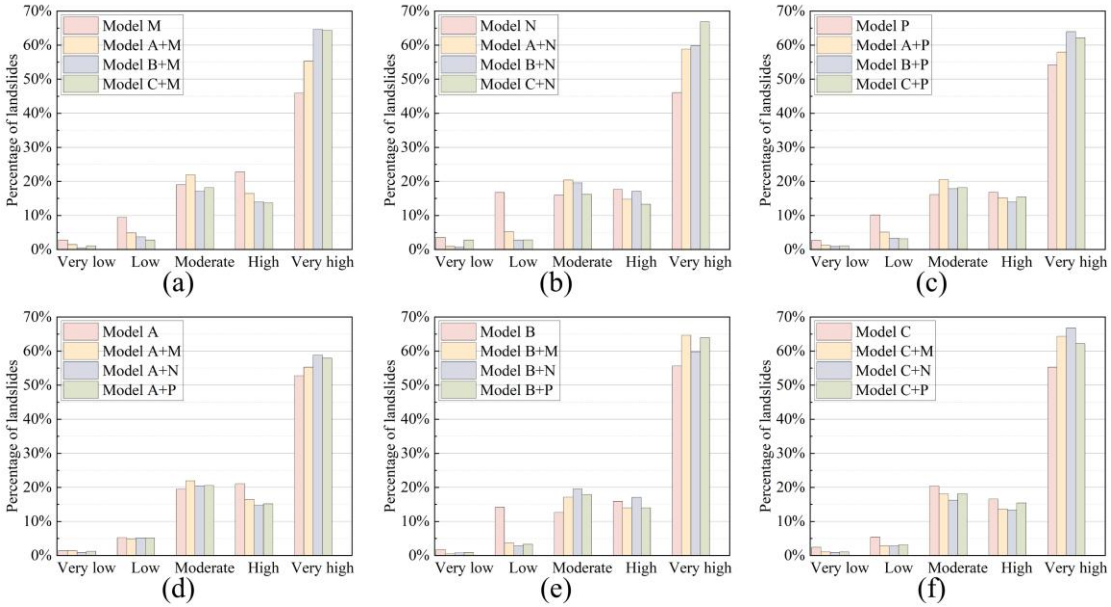

Fig. 12. Percentage of landslides within each susceptibility class for the baseline and corresponding LGSCF-based models: (a) Model M and its LGSCF combinations, (b) Model N and its LGSCF combinations, (c) Model P and its LGSCF combinations, (d) Model A and its LGSCF combinations, (e) Model B and its LGSCF combinations, (f) Model C and its LGSCF combinations. The LGSCF-based models generally show higher proportions of landslides in the "very high" class and lower proportions in the "very low" class. Further details of the baseline models and their corresponding LGSCF combinations are provided in Tables 3 and 4.

5.2 Robustness and additional regional evaluation

To further assess the robustness and spatial generalisability of the results, a five-fold spatial robustness analysis was conducted using the original experimental fold and four additional spatially partitioned folds. Identical fold configurations were applied to all models. Fold-wise AUC values were summarised using the mean, standard deviation, and t-based 95% confidence interval. As each LGSCF-based model and its corresponding spatial-context baselines (Model A, B, or C) were evaluated using the same folds, paired t-tests were used to assess whether the observed AUC improvements were statistically significant.

The five-fold results were broadly consistent with the original random-split evaluation (Fig. 13), and Model B+M remained the best-performing combination, achieving a mean AUC of 0.9506. All nine LGSCF-based models achieved higher mean AUC values than their corresponding spatial-context baselines. Eight of the nine LGSCF-based models exhibited lower standard deviations (SD) than their corresponding spatial-context baselines, indicating that their AUC values were generally less sensitive to changes in the spatial data partition. Seven combinations showed statistically significant improvements at $p < 0.05$,

the gains for Model B+P ($p = 0.1699$) and Model C+N ($p = 0.1233$) were not significant, indicating that the benefit of LGSCF is not equally strong for every branch pairing.

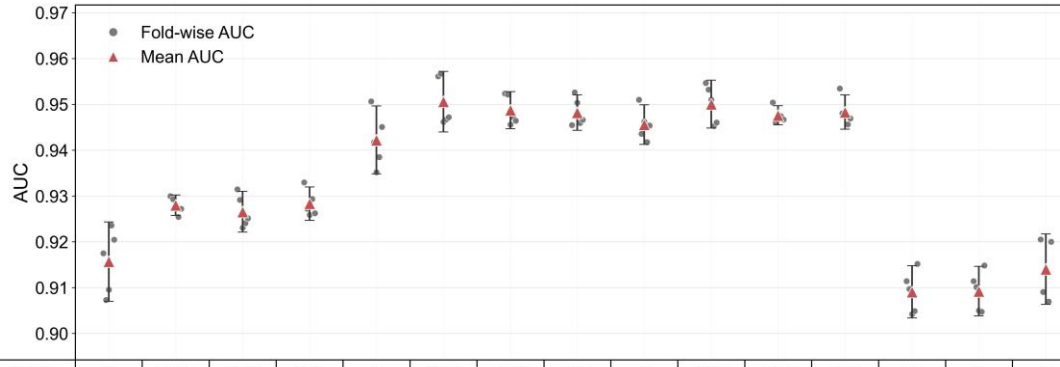

Model	A	A+M	A+N	A+P	B	B+M	B+N	B+P	C	C+M	C+N	C+P	M	N	P
Mean	0.9157	0.9280	0.9265	0.9283	0.9422	0.9506	0.9487	0.9482	0.9456	0.9500	0.9476	0.9483	0.9091	0.9092	0.9140
SD	0.0070	0.0018	0.0036	0.0029	0.0060	0.0053	0.0033	0.0031	0.0035	0.0042	0.0017	0.0030	0.0046	0.0043	0.0062
Paired t-test	-	0.0288	0.0442	0.0121	-	0.0195	0.0344	0.1699	-	0.0386	0.1233	0.0123	-	-	-

Fig. 13. AUC values under 5-fold spatial cross-validation. Error bars indicate the 95% confidence intervals. The table reports the mean AUC, standard deviation, and paired t-test p-values. Paired t-tests were conducted with the corresponding baseline model as the reference: Model A for Models A+M, A+N, and A+P; Model B for Models B+M, B+N, and B+P; and Model C for Models C+M, C+N, and C+P. Therefore, p-values are reported only for the LGSCF-based models.

In addition, to assess whether the effectiveness of the LGSCF framework could be reproduced beyond the primary study area, an evaluation was conducted at an additional study site located in Hualien County. The Hualien experiment followed the same modelling procedure as that used for the primary study area, including consistent data sources and the same set of 15 LCFs, as well as identical strategies for non-landslide sampling and dataset construction. Although the overall predictive performance in Hualien was lower than that obtained in the primary study area, the relative advantage of LGSCF was largely preserved (Fig. 14). All nine LGSCF-based models achieved higher AUC values than their corresponding baselines. F1-scores also increased for eight of the nine combinations, with only Model C+N showing a slight decrease of 0.06 percentage points. These results indicate that the performance gains associated with integrating local geo-environmental characteristics and spatial context were not confined to the Nantou study area. Together with the cross-validation, this additional evaluation provides further evidence for the robustness and broader applicability of the LGSCF framework, although the magnitude and statistical significance of its benefits varied among different combinations.

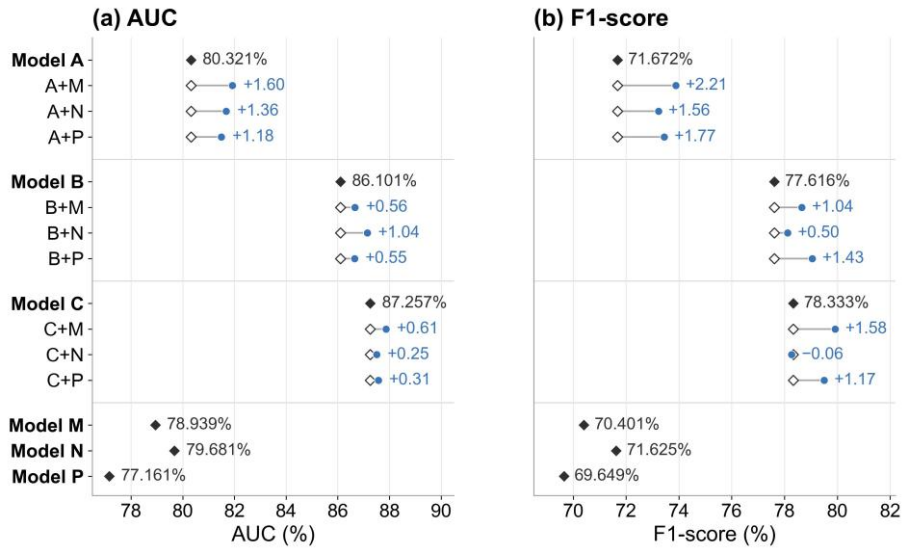

Fig. 14. Evaluation of the LGSCF framework in the additional study area of Hualien County in terms of (a) AUC and (b) F1-score.

5.3 Mechanism analysis

As demonstrated in the results section, the LGSCF strategy consistently improved model performance and enhanced the LSM task. This gain can be largely attributed to the complementary information captured by the spatial-context and local-geo branches. The spatial-context branch learns neighbourhood morphology, slope continuity, and geomorphic context, while the local-geo branch focuses on point-level features that are strongly associated with landslide initiation. LGSCF enables pixel-level cues to adaptively modulate spatial features, allowing the model to selectively emphasise informative regional patterns when local instability signals are present. In this way, the interaction supplements spatial context and helps mitigate cases where spatial features alone may be ambiguous or not directly relevant to landslide occurrence.

To further clarify the mechanism of LGSCF, Table 8 compares several approaches according to how local-geo and spatial context information are modelled and integrated. Pixel-based CNN1D models explicitly extract the LCF characteristics of the target location but do not incorporate neighbourhood information, whereas patch-based CNNs capture spatial context while implicitly mixing the target location with surrounding features. Attention-enhanced CNNs further recalibrate contextual representations, but the local and contextual information remain within the same feature stream. Dual-branch approaches preserve the two representations separately. However, direct concatenation does not explicitly account for the relationship between the two feature representations. The spatial-context branch already incorporates information from the target pixel, while the two branches encode information at different spatial scopes. Simply stacking their features leaves both the overlapping information and the cross-branch relationship to be resolved implicitly by

subsequent layers. In contrast, LGSCF establishes an explicit directional interaction, using local-geo features to modulate the spatial-context representation through feature-wise scaling and shifting.

Table 8. Comparison of representative local-geo, spatial-context, and feature-integration strategies in LSM.

Method	Input	Local information modelling	Spatial-context modelling	Local-geo and spatial context integration
Pixel-based CNN1D	Target pixel LCF vector	Explicit point-level feature extraction	Not included	None
Patch-based CNN (CNN2D and CNN3D)	LCF patch	Implicit; target-location information is embedded in the patch	Convolutional extraction	Implicit mixing during convolution and pooling
Attention-enhanced CNN (e.g., CBAM)	LCF patch	Implicit within the contextual representation	Convolution with channel/spatial feature recalibration	Within-stream feature recalibration
Dual-branch concatenation	Target pixel LCF vector + LCF patch	Separate local feature extraction	Separate spatial-context feature extraction	Direct concatenation of local and contextual features
Proposed LGSCF	Target pixel LCF vector + LCF patch	Separate local feature extraction	Separate spatial-context feature extraction	FiLM-based directional modulation

To examine whether this conceptual distinction is reflected in model performance, an additional experiment was conducted using Model A as the spatial-context branch and Models M, N, and P as the respective local-geo branches, with direct concatenation replacing the proposed FiLM-based fusion. The corresponding LGSCF results were taken from the runs shown in Fig. 9 for comparison. As shown in Fig. 15, the three concatenation-based combinations achieved AUC values comparable to those of the corresponding local-geo branches but did not outperform the spatial-context baseline (Model A). A similar pattern was observed for F1-score, for which concatenation provided only limited improvement, with only Concatenation A+M exceeding Model A and the corresponding LGSCF variant. These results suggest that simply increasing the amount of feature information does not necessarily lead to an effective fusion and may provide little or even adverse benefit relative to the stronger constituent branch. Moreover, the varying gains among different LGSCF combinations indicate that fusion performance is not determined solely by the predictive strength of the individual branches, but also by how effectively their

complementary representations are coordinated.

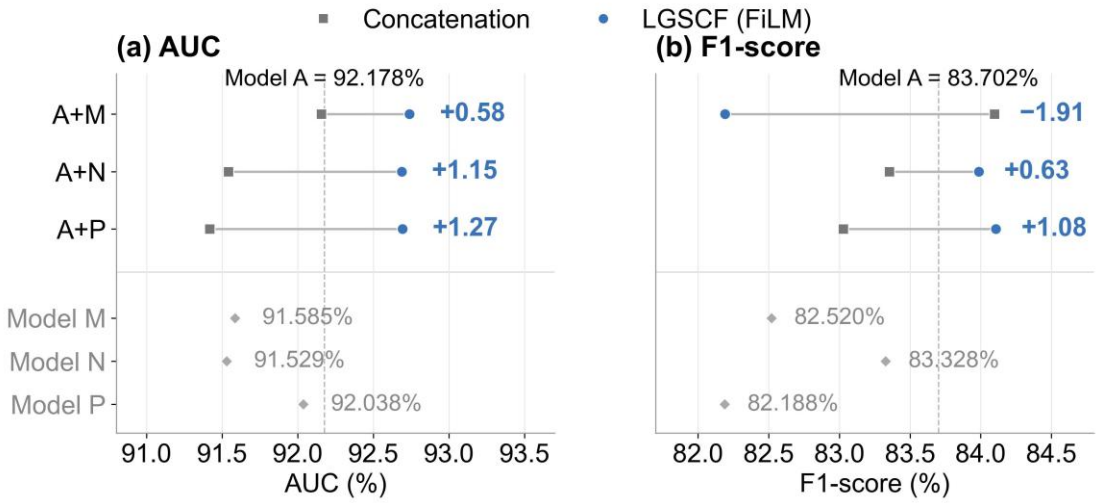

Fig. 15. Comparison of direct concatenation and FiLM-based LGSCF in terms of (a) AUC and (b) F1-score.

5.4 Limitations and future work

Several limitations of the LGSCF framework should be acknowledged. First, although the performance gains using the LGSCF strategy were clearly observed, the contributions of individual FiLM components were not quantitatively isolated. Future work could therefore conduct finer-grained ablation experiments, including scaling-only and shifting-only configurations, to further clarify the respective roles of these components. Second, for baseline models with already strong performance (e.g., Model C), the improvement brought by LGSCF becomes relatively modest. This raised a potential need to investigate how the strategy behaves when using more advanced architectures as one of the branches, and whether additional refinement or adaptive mechanisms may be required under such settings. Third, while LGSCF generally enhanced overall prediction capability, the improvement across positive and negative classes was not always symmetric. This imbalance might stem from characteristics inherited from the baselines, suggesting that future work could explore strategies to further enhance class-balanced prediction performance. Finally, the framework was evaluated in a single study area. Finally, although the additional evaluation in Hualien County showed that the performance gains of LGSCF could be reproduced beyond the primary study area, both study areas are located in Taiwan and therefore represent a relatively limited geographical context. Further evaluation in regions with more distinct geological, climatic, and landslide conditions is still required to establish the broader applicability of the framework.

In addition, LGSCF is subject to several sources of uncertainty commonly encountered in LSM. For instance, the 11 Ĭ 11 patch size was selected according to the typical landslide extent within the study area and the spatial resolution of the LCFs. However, different patch sizes may change the amount

of neighbourhood information captured by the model and consequently affect its performance, which requires further investigation [83]. Non-landslide samples were selected using the FR method. Although this approach reduces the likelihood of incorrectly labelling potential landslide locations as stable terrain, it may favour negative samples that are environmentally distinct from landslide locations. Various alternative methods for selecting non-landslide samples have been investigated in previous studies [68,69,84ï 86], but which method is most suitable for the proposed strategy remains unclear. The landslide inventory also introduces potential uncertainty through omissions, positional inaccuracies, temporal mismatches with the conditioning-factor data, and the simplification involved in representing landslide areas using selected sample locations [55,87]. Future work should therefore examine the sensitivity of LGSCF to different patch sizes and negative-sample selection strategies and evaluate the framework using multi-temporal and field-validated landslide inventories.

6 Conclusion

This study proposed the LGSCF strategy, which integrates dual-branch CNNs through a feature-wise modulation mechanism to jointly capture local-geo characteristics of landslide or non-landslide locations and neighbourhood spatial context in LSM. Instead of defining a single deep learning network structure, LGSCF provides a flexible framework that can be applied to integrate different CNN architectures, allowing for broad adaptability.

Six baseline models were used to validate the effectiveness of the LGSCF strategy. The experimental results show consistent improvements in LSM accuracy using the LGSCF-based models over their single-branch counterparts. In particular, the LGSCF-based models achieved higher F1-scores and AUC values, and showed a more pronounced concentration of landslides in the very high susceptibility category. The cross-validation and additional evaluation in Hualien County demonstrated the robustness and reproducibility of the LGSCF strategy. These findings demonstrate that synergising local geo-environmental characteristics with spatial context yielded more accurate predictions. From a practical perspective, these outcomes suggest that existing CNN-based LSM models can be readily enhanced by incorporating the LGSCF strategy, offering improved predictive accuracy. Nevertheless, although the additional Hualien evaluation extends the assessment beyond the primary study area, both study areas are located in Taiwan, and further evaluation under more diverse geological, climatic, and landslide conditions remains necessary to assess the broader applicability of the proposed framework. It is also valuable to systematically examine which data characteristics, model structures, or parameter settings most strongly influence the effectiveness of the proposed strategy. Such efforts can help refine the framework and maximise its benefits.

Author contributions

Y.C.: Conceptualisation, methodology, software, formal analysis, data curation, investigation, visualisation, writing - original draft, writingð review and editing. **L.F.**: Conceptualisation, methodology, software, formal analysis, data curation, investigation, supervision, writingð review and editing. **Q.Z.**: Conceptualisation, methodology, formal analysis, data curation, software, investigation, writingð review and editing. **C.Z.**: Conceptualisation, methodology, formal analysis, investigation, writingð review and editing. **Y.L.**: Conceptualisation, writingð review and editing. **R.M.**: Conceptualisation, writingð review and editing.

Funding

This research was supported by the Xiâan Jiaotong-Liverpool University Postgraduate Research Scholarship under Grant FOSA2312049.

Data availability

The datasets used and/or analysed during the current study will be made available from the corresponding author on reasonable request.

Declarations

Ethical approval

Not applicable.

Consent to participate

Not applicable.

Consent to publications

Not applicable.

Declaration of competing interest

The authors declare that they have no competing interests or other interests that might be perceived to influence the results and/or discussion reported in this paper.

Appendix A

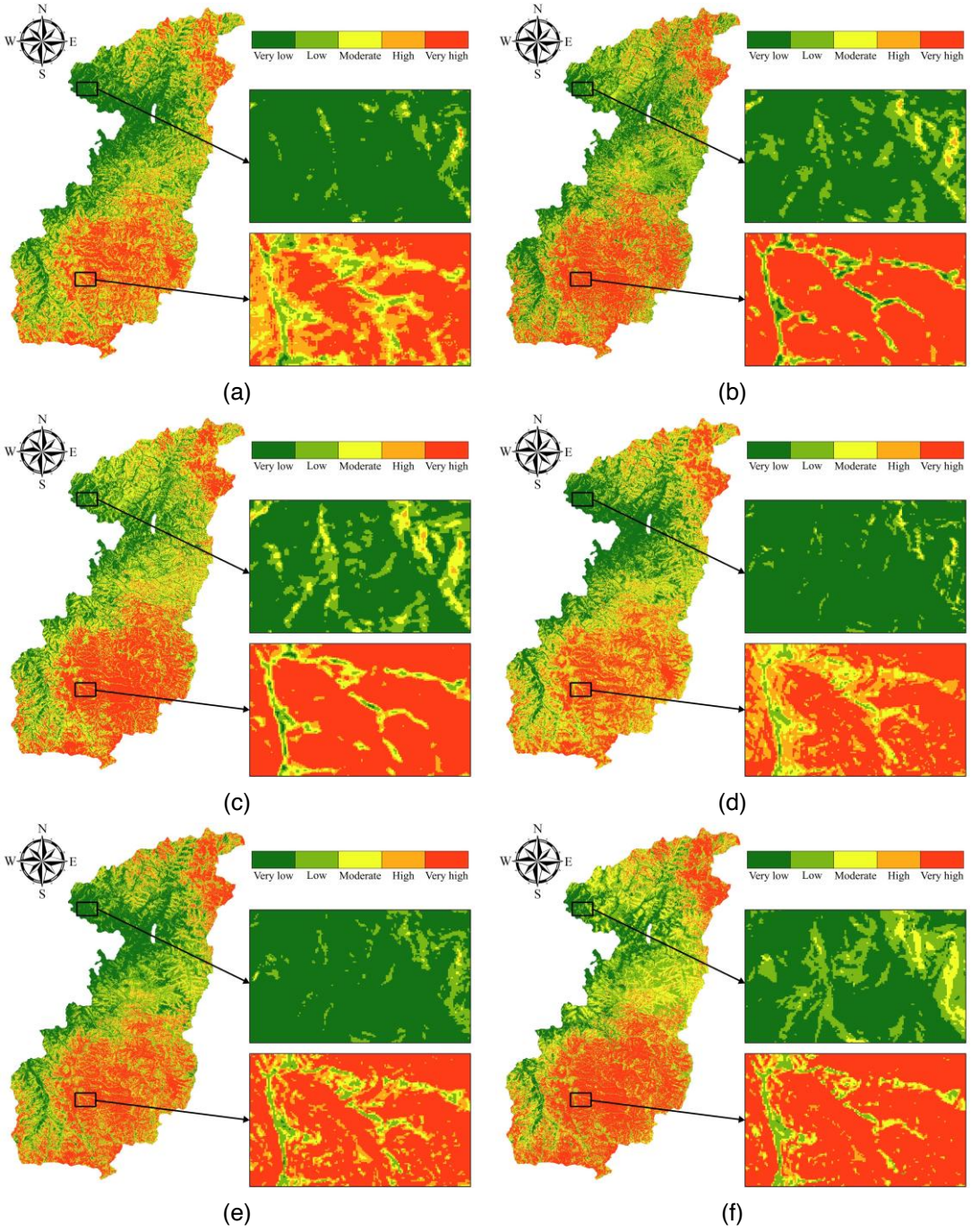

Fig. A1. Landslide susceptibility maps produced by six base models: (a) Model A, (b) Model B, (c) Model C, (d) Model M, (e) Model N, and (f) Model P.

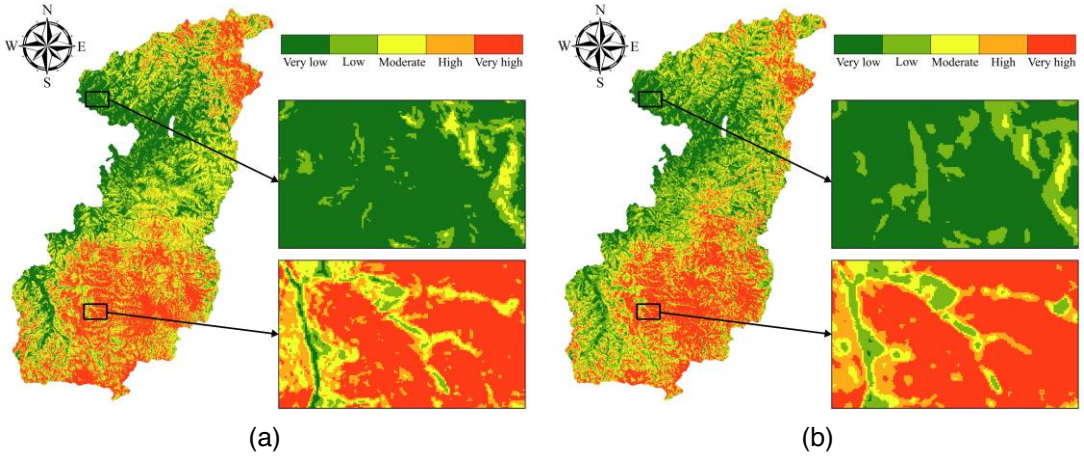
N
W
E
S
Very low
Low
Moderate
High
Very high

(a)

N
W
E
S
Very low
Low
Moderate
High
Very high

(b)

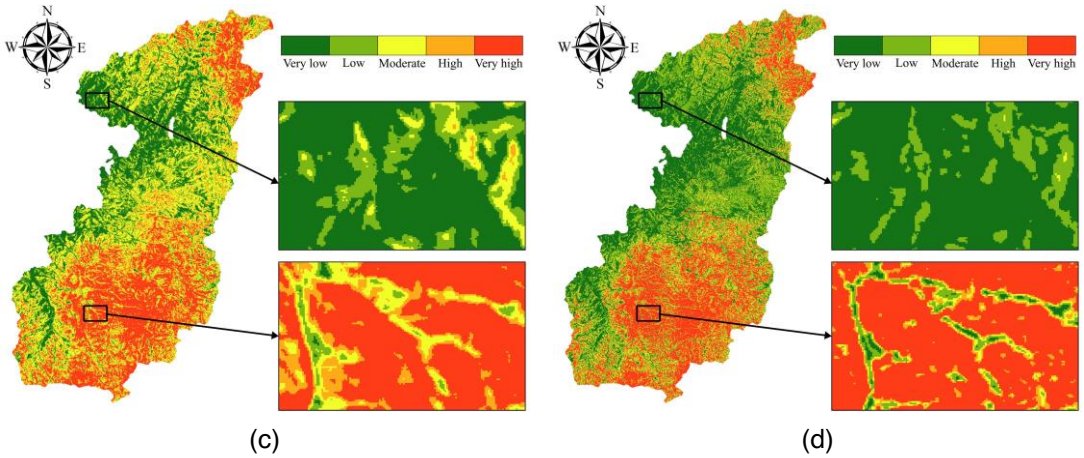
N
W
E
S
Very low
Low
Moderate
High
Very high

(c)

N
W
E
S
Very low
Low
Moderate
High
Very high

(d)

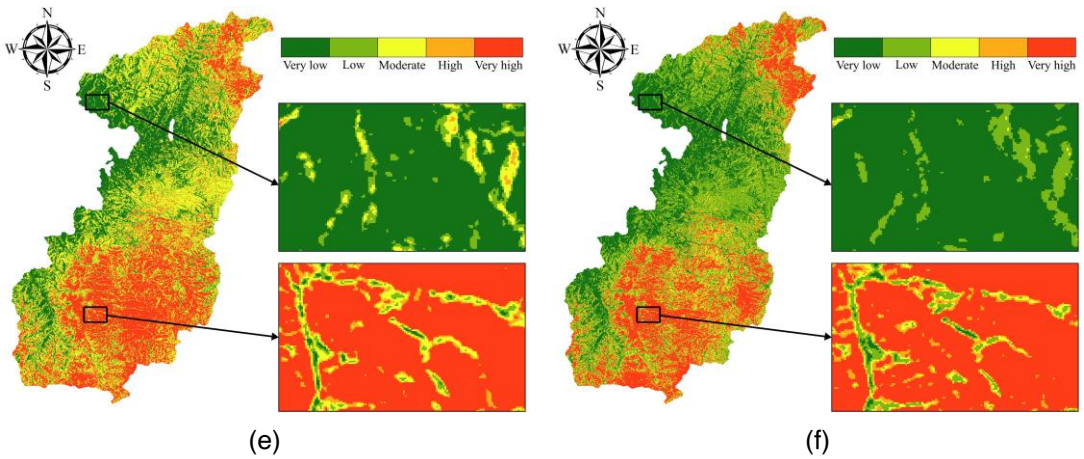
N
W
E
S
Very low
Low
Moderate
High
Very high

(e)

N
W
E
S
Very low
Low
Moderate
High
Very high

(f)

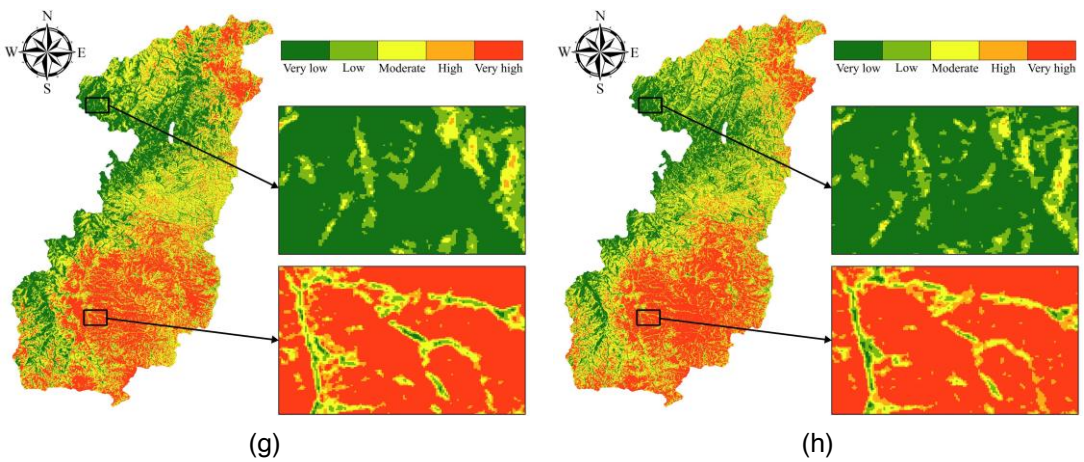
N
W
E
S
Very low
Low
Moderate
High
Very high

(g)

N
W
E
S
Very low
Low
Moderate
High
Very high

(h)

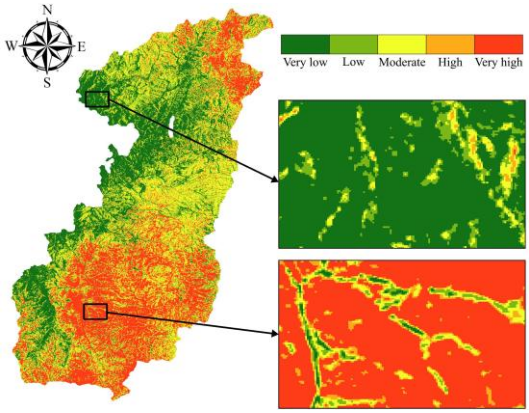

(i)

Fig. A2. Landslide susceptibility maps produced by nine LGSCF-based models: (a) Model A+M, (b) Model A+N, (c) Model A+P, (d) Model B+M, (e) Model B+N, (f) Model B+P, (g) Model C+M, (h) Model C+N, and (i) Model C+P.

Appendix B

Table B1. Hardware configuration, training time, and computational complexity of the baseline and LGSCF models.

Items	M	N	P	A	B	C	A+M	A+N	A+P	B+M	B+N	B+P	C+M	C+N	C+P
Time (s)	177.58	287.08	161.69	291.36	187.69	177.82	300.93	232.91	240.40	170.31	148.69	132.01	143.53	140.49	145.42
Parameters	6252	6514	1113890	150596	77980	39618	197637	214602	490234	93000	129336	249876	80742	112210	238946
FLOPs	14882	20642	5862818	1536830	2209676	2024130	2549015	2861855	14847306	2241696	2319604	10568108	2108310	2176482	10377378
CPU	AMD EPYC 7282 16-Core Processor														
GPU	NVIDIA GeForce RTX 4090 D (24 GB VRAM)														
Memory	128 GB														
Hard disk	2 TB														

Notes: An early-stopping strategy with a patience of 10 epochs was applied during training. Specifically, training was terminated when the monitored validation performance did not improve for 10 consecutive epochs. Therefore, the reported training time represents the total time required for each model to reach its stopping condition, rather than the time required to complete a fixed number of epochs. The generally higher computational complexity of the LGSCF-based models is primarily attributable to their dual-branch architecture. Unlike the single-branch baselines, each LGSCF-based model simultaneously employs the feature-extraction components of its two corresponding baseline models. One branch preserves the characteristics of the pixel directly associated with the sample label, whereas the other extracts complementary spatial context from the surrounding neighbourhood. The features generated by the two branches are subsequently integrated through additional feature fusion operations. Such parallel feature extraction and subsequent fusion inevitably require additional computational operations and, in most cases, introduce additional trainable parameters. Despite this increase in theoretical complexity, the observed training times of the LGSCF models remained within a range comparable to those of the corresponding baseline models, without imposing a substantial additional training burden. This indicates that the integration of local-geo characteristics and neighbourhood context can be achieved at an acceptable computational cost, supporting the computational practicality and architectural rationality of the proposed LGSCF strategy.

References

1. Hungr O, Leroueil S, Picarelli L. The Varnes classification of landslide types, an update. Landslides. 2014;11:167–94. https://doi.org/10.1007/s10346-013-0436-y

2. Vargas-Cuervo G, Hernández-Peña YT, Zafra-Mejía CA. Challenges for Sustainable Urban Planning: A Spatiotemporal Analysis of Complex Landslide Risk in a Latin American Megacity. Sustainability. 2024;16:3133. https://doi.org/10.3390/su16083133

3. Li BV, Jenkins CN, Xu W. Strategic protection of landslide vulnerable mountains for biodiversity conservation under land-cover and climate change impacts. Proc Natl Acad Sci. 2022;119:e2113416118. https://doi.org/10.1073/pnas.2113416118

4. Remondo J, Sánchez-Díaz M, Cuesta-Albertos JA. An Increasing Trend of Landslides as a Consequence of the Global Change. Earth Syst Environ [Internet]. 2025 [cited 2025 Sept 17]; https://doi.org/10.1007/s41748-025-00685-0

5. Xiao S, Zhang L, Xiao T, Jiang R, Peng D, Lu W, et al. Landslide Damming Threats Along the Jinsha River, China. Engineering. 2024;42:326–39. https://doi.org/https://doi.org/10.1016/j.eng.2024.07.001

6. Kumar P. Social and Economic Impact in the Landslide Prone Zones and Related Policies. In: Chatterjee U, Lalmalsawmzauva KC, Biswas B, Pal SC, editors. Landslides Himal Reg Risk Assess Mitig Strategy Sustain Manag [Internet]. Singapore: Springer Nature Singapore; 2024. p. 499–529. https://doi.org/10.1007/978-981-97-4680-4_22

7. Dahl M-PJ, Mortensen LE, Veihe A, Jensen NH. A simple qualitative approach for mapping regional landslide susceptibility in the Faroe Islands. Nat Hazards Earth Syst Sci. 2010;10:159–70. https://doi.org/10.5194/nhess-10-159-2010

8. Foumelis M, Lekkas E, Parcharidis I. LANDSLIDE SUSCEPTIBILITY MAPPING BY GIS-BASED QUALITATIVE WEIGHTING PROCEDURE IN CORINTH AREA. Bull Geol Soc Greece. 2018;36:904–12. https://doi.org/10.12681/bgsg.16840

9. Zhu A-X, Wang R, Qiao J, Qin C-Z, Chen Y, Liu J, et al. An expert knowledge-based approach to landslide susceptibility mapping using GIS and fuzzy logic. Geomorphology. 2014;214:128–38. https://doi.org/https://doi.org/10.1016/j.geomorph.2014.02.003

10. Myronidis D, Papageorgiou C, Theophanous S. Landslide susceptibility mapping based on landslide history and analytic hierarchy process (AHP). Nat Hazards. 2016;81:245–63. https://doi.org/10.1007/s11069-015-2075-1

11. Dai K, Chen C, Shi X, Wu M, Feng W, Xu Q, et al. Dynamic landslides susceptibility

evaluation in Baihetan Dam area during extensive impoundment by integrating geological model and InSAR observations. Int J Appl Earth Obs Geoinformation. 2023;116:103157. https://doi.org/10.1016/j.jag.2022.103157

12. Yao Z, Chen M, Zhan J, Zhuang J, Sun Y, Yu Q, et al. Refined Landslide Susceptibility Mapping by Integrating the SHAP-CatBoost Model and InSAR Observations: A Case Study of Lishui, Southern China. Appl Sci. 2023;13:12817. https://doi.org/10.3390/app132312817

13. Nguyen HD, Nguyen QH, Du QVV, Pham VT, Pham LT, Van Hoang T, et al. Landslide susceptibility prediction using machine learning and remote sensing: Case study in Thua Thien Hue province, Vietnam. Geol J. 2024;59:636–58. https://doi.org/10.1002/gj.4885

14. Marin RJ, Velásquez MF, Sánchez O. Applicability and performance of deterministic and probabilistic physically based landslide modeling in a data-scarce environment of the Colombian Andes. J South Am Earth Sci. 2021;108:103175. https://doi.org/10.1016/j.jsames.2021.103175

15. Rana H, Babu GLS. Regional back analysis of landslide events using TRIGRS model and rainfall threshold: an approach to estimate landslide hazard for Kodagu, India. Bull Eng Geol Environ. 2022;81:160. https://doi.org/10.1007/s10064-022-02660-9

16. Grant A, Wartman J, Abou-Jaoude G. Multimodal method for coseismic landslide hazard assessment. Eng Geol. 2016;212:146–60. https://doi.org/https://doi.org/10.1016/j.enggeo.2016.08.005

17. Li Y, Rangarajan S, Cheng Y, Rahardjo H, Satyanaga A. Random forest-based prediction of shallow slope stability considering spatiotemporal variations in unsaturated soil moisture. Sci Rep. 2025;15:8751. https://doi.org/10.1038/s41598-025-92739-6

18. Hussain S, Hongxing S, Ali M, Sajjad MM, Ali M, Afzal Z, et al. Optimized landslide susceptibility mapping and modelling using PS-InSAR technique: a case study of Chitral valley, Northern Pakistan. Geocarto Int. 2022;37:5227–48. https://doi.org/10.1080/10106049.2021.1914750

19. Zhang J, Gao B, Huang H, Chen L, Li Y, Yang D. SBAS-InSAR-Based Landslide Susceptibility Mapping Along the North Lancang River, Tibetan Plateau. Front Earth Sci. 2022;10:901889. https://doi.org/10.3389/feart.2022.901889

20. Zhu Z, Gan S, Yuan X, Zhang J. Landslide Susceptibility Mapping with Integrated SBAS-InSAR Technique: A Case Study of Dongchuan District, Yunnan (China). Sensors. 2022;22:5587. https://doi.org/10.3390/s22155587

21. Chen L, Ma P, Yu C, Zheng Y, Zhu Q, Ding Y. Landslide susceptibility assessment in

multiple urban slope settings with a landslide inventory augmented by InSAR techniques. Eng Geol. 2023;327:107342. https://doi.org/10.1016/j.enggeo.2023.107342

22. Lee S, Lee M-J, Jung H-S, Lee S. Landslide susceptibility mapping using Naïve Bayes and Bayesian network models in Umyeonsan, Korea. Geocarto Int. Taylor & Francis; 2020;35:1665–79. https://doi.org/10.1080/10106049.2019.1585482

23. Lin Y-T, Chen Y-K, Yang K-H, Chen C-S, Han J-Y. Integrating InSAR Observables and Multiple Geological Factors for Landslide Susceptibility Assessment. Appl Sci. 2021;11:7289. https://doi.org/10.3390/app11167289

24. Hussain MA, Chen Z, Wang R, Shoaib M. PS-InSAR-Based Validated Landslide Susceptibility Mapping along Karakorum Highway, Pakistan. Remote Sens. 2021;13:4129. https://doi.org/10.3390/rs13204129

25. Xiao B, Zhao J, Li D, Zhao Z, Zhou D, Xi W, et al. Combined SBAS-InSAR and PSO-RF Algorithm for Evaluating the Susceptibility Prediction of Landslide in Complex Mountainous Area: A Case Study of Ludian County, China. Sensors. 2022;22:8041. https://doi.org/10.3390/s22208041

26. Adnan MSG, Rahman MS, Ahmed N, Ahmed B, Rabbi MdF, Rahman RM. Improving Spatial Agreement in Machine Learning-Based Landslide Susceptibility Mapping. Remote Sens. 2020;12:3347. https://doi.org/10.3390/rs12203347

27. Yang N, Wang R, Liu Z, Yao Z. Landslide susceptibility prediction improvements based on a semi-integrated supervised machine learning model. Environ Sci Pollut Res. 2023;30:50280–94. https://doi.org/10.1007/s11356-023-25650-0

28. Li X, Nishio M, Sugawara K, Iwanaga S, Chun P. Surrogate Model Development for Slope Stability Analysis Using Machine Learning. Sustainability. 2023;15:10793. https://doi.org/10.3390/su151410793

29. Wang G, Zhao B, Wu B, Zhang C, Liu W. Intelligent prediction of slope stability based on visual exploratory data analysis of 77 in situ cases. Int J Min Sci Technol. 2023;33:47–59. https://doi.org/10.1016/j.ijmst.2022.07.002

30. Youssef K, Shao K, Moon S, Bouchard L -s. Landslide susceptibility modeling by interpretable neural network. Commun EARTH Environ. 2023;4. https://doi.org/10.1038/s43247-023-00806-5

31. Lin S, Liang Z, Zhao S, Dong M, Guo H, Zheng H. A comprehensive evaluation of ensemble machine learning in geotechnical stability analysis and explainability. Int J Mech Mater Des. 2024;20:331–52. https://doi.org/10.1007/s10999-023-09679-0

32. Wang Y, Fang Z, Hong H. Comparison of convolutional neural networks for landslide susceptibility mapping in Yanshan County, China. Sci Total Environ. 2019;666:975–93. https://doi.org/10.1016/j.scitotenv.2019.02.263

33. Zhang S, Bai L, Li Y, Li W, Xie M. Comparing Convolutional Neural Network and Machine Learning Models in Landslide Susceptibility Mapping: A Case Study in Wenchuan County. Front Environ Sci. 2022;10:886841. https://doi.org/10.3389/fenvs.2022.886841

34. Chen C, Fan L. An Attribution Deep Learning Interpretation Model for Landslide Susceptibility Mapping in the Three Gorges Reservoir Area. IEEE Trans Geosci Remote Sens. 2023;61:1–15. https://doi.org/10.1109/TGRS.2023.3323668

35. Chen C, Fan L. Interpretability of Statistical, Machine Learning, and Deep Learning Models for Landslide Susceptibility Mapping in Three Gorges Reservoir Area [Internet]. arXiv; 2024 [cited 2025 May 8]. https://doi.org/10.48550/arXiv.2405.11762

36. Fang Z, Wang Y, Peng L, Hong H. Integration of convolutional neural network and conventional machine learning classifiers for landslide susceptibility mapping. Comput Geosci. Elsevier BV; 2020;139:104470. https://doi.org/10.1016/j.cageo.2020.104470

37. Youssef AM, Pradhan B, Dikshit A, Al-Katheri MM, Matar SS, Mahdi AM. Landslide susceptibility mapping using CNN-1D and 2D deep learning algorithms: comparison of their performance at Asir Region, KSA. Bull Eng Geol Environ. 2022;81:165. https://doi.org/10.1007/s10064-022-02657-4

38. Lu J, He Y, Zhang L, Zhang Q, Tang J, Huo T, et al. A Synergistic CNN-DF Method for Landslide Susceptibility Assessment. IEEE J Sel Top Appl Earth Obs Remote Sens. 2025;18:6584–99. https://doi.org/10.1109/JSTARS.2025.3541638

39. Azarafza M, Azarafza M, Akgün H, Atkinson PM, Derakhshani R. Deep learning-based landslide susceptibility mapping. Sci Rep. 2021;11:24112. https://doi.org/10.1038/s41598-021-03585-1

40. Wang H, Zhang L, Luo H, He J, Cheung RWM. AI-powered landslide susceptibility assessment in Hong Kong. Eng Geol. 2021;288:106103. https://doi.org/10.1016/j.enggeo.2021.106103

41. Huang W, Ding M, Li Z, Yu J, Ge D, Liu Q, et al. Landslide susceptibility mapping and dynamic response along the Sichuan-Tibet transportation corridor using deep learning algorithms. CATENA. 2023;222:106866. https://doi.org/10.1016/j.catena.2022.106866

42. Bao S, Liu J, Wang L, Zhao X. Application of Transformer Models to Landslide Susceptibility Mapping. Sensors. 2022;22:9104. https://doi.org/10.3390/s22239104

43. Bao S, Liu J, Wang L, Konečný M, Che X, Xu S, et al. Landslide Susceptibility Mapping by Fusing Convolutional Neural Networks and Vision Transformer. Sensors. 2022;23:88. https://doi.org/10.3390/s23010088

44. Zhao Z, Chen T, Dou J, Liu G, Plaza A. Landslide Susceptibility Mapping Considering Landslide Local-Global Features Based on CNN and Transformer. IEEE J Sel Top Appl Earth Obs Remote Sens. 2024;17:7475–89. https://doi.org/10.1109/JSTARS.2024.3379350

45. Zeng H, Zhu ,Qing, Ding ,Yulin, Hu ,Han, Chen ,Li, Xie ,Xiao, et al. Graph neural networks with constraints of environmental consistency for landslide susceptibility evaluation. Int J Geogr Inf Sci. Taylor & Francis; 2022;36:2270–95. https://doi.org/10.1080/13658816.2022.2103819

46. Zhang Q, He Y, Zhang L, Lu J, Gao B, Yang W, et al. A landslide susceptibility assessment method considering the similarity of geographic environments based on graph neural network. Gondwana Res. 2024;132:323–42. https://doi.org/10.1016/j.gr.2024.04.013

47. Lei X, Liu H, Chen Z, Li S, Chen H, Zeng S, et al. Investigating the landslide susceptibility assessment methods for multi-scale slope units based on SDGSAT-1 and Graph Neural Networks. Int J Digit Earth. 2025;18:2468913. https://doi.org/10.1080/17538947.2025.2468913

48. Li J, Hong D, Gao L, Yao J, Zheng K, Zhang B, et al. Deep learning in multimodal remote sensing data fusion: A comprehensive review. Int J Appl Earth Obs Geoinformation. 2022;112:102926. https://doi.org/10.1016/j.jag.2022.102926

49. Woo S, Park J, Lee J-Y, Kweon IS. CBAM: Convolutional Block Attention Module. In: Ferrari V, Hebert M, Sminchisescu C, Weiss Y, editors. Comput Vis – ECCV 2018 [Internet]. Cham: Springer International Publishing; 2018 [cited 2026 July 14]. p. 3–19. https://doi.org/10.1007/978-3-030-01234-2_1

50. Roy SK, Deria A, Hong D, Rasti B, Plaza A, Chanussot J. Multimodal Fusion Transformer for Remote Sensing Image Classification. IEEE Trans Geosci Remote Sens. 2023;61:1–20. https://doi.org/10.1109/TGRS.2023.3286826

51. Peel MC, Finlayson BL, McMahon TA. Updated world map of the Köppen-Geiger climate classification. Hydrol Earth Syst Sci. 2007;11:1633–44. https://doi.org/10.5194/hess-11-1633-2007

52. Lin C-Y, Cheng K-H. Relationship Between Debris Flow and Precipitation From Nantou and Chiayi County in Taiwan. Trans Sci Technol. 2019;6:340–52.

53. Lin J-Y, Chao J-C, Wu C-L, Hsieh W-F. Extreme-rainfall Data as a Basis for Landslide

Warnings: a Case Study of a Road in Central Taiwan. IOP Conf Ser Earth Environ Sci. IOP Publishing; 2021;798:012018. https://doi.org/10.1088/1755-1315/798/1/012018

54. Wu BS, Chuang RY, Chen Y-C, Lin Y-S. Characteristics of landslides triggered by the 2013 ML6.5 Nantou, Taiwan, earthquake. Earth Planets Space. 2022;74:7. https://doi.org/10.1186/s40623-021-01560-8

55. Huang F, Li R, Catani F, Zhou X, Zeng Z, Huang J. Uncertainties in landslide susceptibility prediction: Influence rule of different levels of errors in landslide spatial position. J Rock Mech Geotech Eng. 2024;16:4177–91. https://doi.org/10.1016/j.jrmge.2024.02.001

56. Ministry of Agriculture. 111 Annual Taiwan Landslide Map Layer ｜ 政府資料開放平臺 [Internet]. 2022 [cited 2025 July 9]. https://data.gov.tw/en/datasets/166846. Accessed 9 July 2025

57. Reichenbach P, Rossi M, Malamud BD, Mihir M, Guzzetti F. A review of statistically-based landslide susceptibility models. Earth-Sci Rev. Elsevier BV; 2018;180:60–91. https://doi.org/10.1016/j.earscirev.2018.03.001

58. Merghadi A, Yunus AP, Dou J, Whiteley J, ThaiPham B, Bui DT, et al. Machine learning methods for landslide susceptibility studies: A comparative overview of algorithm performance. Earth-Sci Rev. 2020;207:103225. https://doi.org/10.1016/j.earscirev.2020.103225

59. Chen C, Fan L. Selection of contributing factors for predicting landslide susceptibility using machine learning and deep learning models. Stoch Environ Res Risk Assess [Internet]. 2023; https://doi.org/10.1007/s00477-023-02556-4

60. Cheng Y, Pang H, Li Y, Fan L, Wei S, Yuan Z, et al. Applications and Advancements of Spaceborne InSAR in Landslide Monitoring and Susceptibility Mapping: A Systematic Review. Remote Sens. 2025;17:999. https://doi.org/10.3390/rs17060999

61. Huang F, Liu K, Jiang S, Catani F, Liu W, Fan X, et al. Optimization method of conditioning factors selection and combination for landslide susceptibility prediction. J Rock Mech Geotech Eng. 2025;17:722–46. https://doi.org/10.1016/j.jrmge.2024.04.029

62. Wen H, Liu B, Di M, Li J, Zhou X. A SHAP-enhanced XGBoost model for interpretable prediction of coseismic landslides. Adv SPACE Res. 2024;74:3826–54. https://doi.org/10.1016/j.asr.2024.07.013

63. Bu X, Fan S, Zhang Z, Zhu K, Ma X. Interpretability study of earthquake-induced landslide susceptibility combining dimensionality reduction and clustering. Front EARTH Sci. 2025;13. https://doi.org/10.3389/feart.2025.1577165

64. Zhang X, Huang S, Gao B. Full-waveform CNN-transformer neural network for regional coseismic landslide susceptibility modeling: A case study of the 2022 Luding earthquake, China. Eng Geol. 2026;362. https://doi.org/10.1016/j.enggeo.2025.108520

65. Yang J, Dong J, Xiao X, Dai J, Wu C, Xia J, et al. Divergent shifts in peak photosynthesis timing of temperate and alpine grasslands in China. Remote Sens Environ. 2019;233:111395. https://doi.org/10.1016/j.rse.2019.111395

66. Potapov P, Hansen MC, Pickens A, Hernandez-Serna A, Tyukavina A, Turubanova S, et al. The Global 2000-2020 Land Cover and Land Use Change Dataset Derived From the Landsat Archive: First Results. Front Remote Sens. 2022;3:856903. https://doi.org/10.3389/frsen.2022.856903

67. Liang Z, Wang C, Khan KUJ. Application and comparison of different ensemble learning machines combining with a novel sampling strategy for shallow landslide susceptibility mapping. Stoch Environ Res Risk Assess. 2021;35:1243–56. https://doi.org/10.1007/s00477-020-01893-y

68. Liu Y, Meng Z, Zhu L, Hu D, He H. Optimizing the Sample Selection of Machine Learning Models for Landslide Susceptibility Prediction Using Information Value Models in the Dabie Mountain Area of Anhui, China. Sustainability. 2023;15:1971. https://doi.org/10.3390/su15031971

69. Huang F, Xiong H, Jiang S-H, Yao C, Fan X, Catani F, et al. Modelling landslide susceptibility prediction: A review and construction of semi-supervised imbalanced theory. Earth-Sci Rev. 2024;250:104700. https://doi.org/10.1016/j.earscirev.2024.104700

70. Lu Z, Liu G, Zhao X, Sun K, Chen Y, Song Z, et al. Landslide susceptibility assessment based on an interpretable coupled FR-RF model: A case study of Longyan City, Fujian Province, Southeast China. CHINA Geol. 2021;8:281–94. https://doi.org/10.31035/cg2024123

71. Liu L-L, Zhang Y-L, Xiao T, Yang C. A frequency ratio–based sampling strategy for landslide susceptibility assessment. Bull Eng Geol Environ. 2022;81:360. https://doi.org/10.1007/s10064-022-02836-3

72. Zhu Y, Sun D, Wen H, Zhang Q, Ji Q, Li C, et al. Considering the effect of non-landslide sample selection on landslide susceptibility assessment. Geomat Nat Hazards Risk. 2024;15:2392778. https://doi.org/10.1080/19475705.2024.2392778

73. Wei X, Gardoni P, Zhang L, Tan L, Liu D, Du C, et al. Improving pixel-based regional landslide susceptibility mapping. Geosci Front. 2024;15:101782. https://doi.org/10.1016/j.gsf.2024.101782

74. Perez E, Strub F, De Vries H, Dumoulin V, Courville A. FiLM: Visual Reasoning with a General Conditioning Layer. Proc AAAI Conf Artif Intell [Internet]. 2018 [cited 2025 Aug 14];32. https://doi.org/10.1609/aaai.v32i1.11671

75. Hu Y, Banerjee B, Prasad S. Label-Efficient Hyperspectral Image Classification via Spectral FiLM Modulation of Low-Level Pretrained Diffusion Features.

76. Yang Z, Xu C, Shao X, Ma S, Li L. Landslide susceptibility mapping based on CNN-3D algorithm with attention module embedded. Bull Eng Geol Environ. 2022;81:412. https://doi.org/10.1007/s10064-022-02889-4

77. Cui H-Z, Tong B, Wang T, Dou J, Ji J. A hybrid data-driven approach for rainfall-induced landslide susceptibility mapping: Physically-based probabilistic model with convolutional neural network. J Rock Mech Geotech Eng. 2024;S167477552400355X. https://doi.org/10.1016/j.jrmge.2024.08.005

78. Alqadhi S, Mallick J, Alkahtani M, Ahmad I, Alqahtani D, Hang HT. Developing a hybrid deep learning model with explainable artificial intelligence (XAI) for enhanced landslide susceptibility modeling and management. Nat Hazards. 2024;120:3719–47. https://doi.org/10.1007/s11069-023-06357-4

79. Moghimi A, Singha C, Fathi M, Pirasteh S, Mohammadzadeh A, Varshosaz M, et al. Hybridizing genetic random forest and self-attention based CNN-LSTM algorithms for landslide susceptibility mapping in Darjiling and Kurseong, India. Quat Sci Adv. 2024;14:100187. https://doi.org/10.1016/j.qsa.2024.100187

80. Abdelkader MM, Csámer Á. Comparative assessment of machine learning models for landslide susceptibility mapping: a focus on validation and accuracy. Nat Hazards. 2025;121:10299–321. https://doi.org/10.1007/s11069-025-07197-0

81. Chen W, Xie X, Peng J, Shahabi H, Hong H, Bui DT, et al. GIS-based landslide susceptibility evaluation using a novel hybrid integration approach of bivariate statistical based random forest method. CATENA. 2018;164:135–49. https://doi.org/10.1016/j.catena.2018.01.012

82. Kusuma RJ, Meilano I, Fitri IH. Landslide Susceptibility Assessment using Analytical Hierarchy Process in West Java. IOP Conf Ser Earth Environ Sci. 2025;1472:012035. https://doi.org/10.1088/1755-1315/1472/1/012035

83. Wei X, Gardoni P, Zhang L, Tan L, Liu D, Du C, et al. Improving pixel-based regional landslide susceptibility mapping. Geosci Front. 2024;15. https://doi.org/10.1016/j.gsf.2024.101782

84. Zhu Y, Sun D, Wen H, Zhang Q, Ji Q, Li C, et al. Considering the effect of non-landslide sample selection on landslide susceptibility assessment. Geomat Nat HAZARDS RISK. 2024;15. https://doi.org/10.1080/19475705.2024.2392778

85. Liu X-D, Xiao T, Zhang S-H, Sun P-H, Liu L-L, Peng Z-W. Comparative study of sampling strategies for machine learning-based landslide susceptibility assessment. Stoch Environ Res Risk Assess. 2024;38:4935–57. https://doi.org/10.1007/s00477-024-02841-w

86. Phan T-A-T, Tran T-L, Huynh N-T. Improving Landslide Susceptibility Mapping via Physics-Informed Non-Landslide Sampling and Optimized Ensemble Learning. Transp Infrastruct Geotechnol. 2026;13. https://doi.org/10.1007/s40515-026-00899-3

87. Huang F, Mao D, Jiang S-H, Zhou C, Fan X, Zeng Z, et al. Uncertainties in landslide susceptibility prediction modeling: A review on the incompleteness of landslide inventory and its influence rules. Geosci Front. 2024;15:101886. https://doi.org/10.1016/j.gsf.2024.101886